Global evolution of flux transfer events along the magnetopause from the dayside to the far tail

Yann Pfau-Kempf[1], Konstantinos Papadakis[1], Markku Alho[1], Markus Battarbee[1], Giulia Cozzani[1,2], Lauri Pänkäläinen[1], Urs Ganse[1], Fasil Kebede[1,3], Jonas Suni[1], Konstantinos Horaites[1], Maxime Grandin[4,1], and Minna Palmroth[1,4]

[1]Department of Physics, University of Helsinki, Helsinki, Finland
[2]LPC2E, CNRS/CNES/University of Orléans, Orléans, France
[3]Department of Physics and Technology, University of Bergen, Bergen, Norway
[4]Finnish Meteorological Institute, Helsinki, Finland

Correspondence: Yann Pfau-Kempf (yann.kempf@helsinki.fi)

Abstract. Magnetic flux ropes are structures of magnetic field rolled-up along a longitudinal axis, which are forming in a variety of magnetised plasmas. In near-Earth space, flux ropes are a manifestation of energy transfer at the magnetopause and in the magnetotail current sheet. We present a new method to detect magnetic flux ropes in large-scale simulations, using only magnetic field line tracing. The method does not require prior identification of structures of interest such as current sheets or

5   null lines, and thus allows one to identify flux ropes of any size and orientation, anywhere in the simulation domain. In this work, the new method is implemented in the hybrid-Vlasov model Vlasiator and demonstrated in global simulations of the terrestrial magnetosphere.

We study the evolution of flux ropes forming during flux transfer events on the dayside magnetopause under southward interplanetary magnetic field. It is found that flux ropes with an axial orientation along the dawn-dusk direction and propagating

10 beyond the cusps will rapidly reconnect with the lobe magnetic field and vanish. In contrast, the flux ropes remaining near the equatorial plane and with an axial orientation along the flow direction, that is tangential to the magnetopause, can maintain their structure and propagate tens of Earth radii down the tail in the absence of a reconnecting shear magnetic field component. These results are a step forward in the global characterisation of flux ropes in and around the magnetosphere, and may help in guiding the search for elusive far-tail flux ropes in satellite measurements.

15 # 1   Introduction

Magnetic flux ropes are structures characterised by axially oriented magnetic field around which twisting magnetic field is wrapped with an increasing angle with respect to the axial direction, reminiscent of fibres twisted in a rope. They have been observed or inferred in a variety of plasma environments especially when magnetic reconnection occurs. They form in the Sun, pierce its surface where they can erupt (e.g., Wang et al., 2017; MacTaggart et al., 2021), and propagate in the solar

20 wind as smaller-scale flux ropes with scale sizes of the order of 10^5 km (e.g., Moldwin et al., 2000; Cartwright and Moldwin, 2010) or large magnetic clouds or interplanetary coronal mass ejections spanning 10^7 km and more (e.g., Janvier et al., 2014).

In the near-Earth environment, dynamic magnetopause reconnection leads to the formation of flux ropes called flux transfer events (FTE), which have been studied extensively ever since their first in situ detection (Haerendel et al., 1978; Russell and Elphic, 1978; Rijnbeek and Cowley, 1984), up to and including large statistical surveys using spacecraft constellations (e.g.,

25 Wang et al., 2006; Lv et al., 2016; Kieokaew et al., 2021). When the magnetotail current sheet disrupts and reconnects, flux ropes form that are usually called plasmoids (see e.g., Eastwood and Kiehas, 2015, for a review), which can also nowadays be studied statistically thanks to extensive observational datasets (e.g., Smith et al., 2024). They also form in the ionospheres of unmagnetised planets and in the magnetospheres of magnetised planets, and have been observed at Mercury (e.g., Slavin et al., 2009; Sun et al., 2016; Zhong et al., 2023), Venus (e.g., Elphic and Russell, 1983; Zhang et al., 2012), Mars (e.g., Brain

30 et al., 2010; Hara et al., 2017a, b; Bowers et al., 2021), Jupiter (e.g., Kronberg et al., 2005; Vogt et al., 2014; Sarkango et al., 2021, 2022) and its moon Ganymede (Romanelli et al., 2022), Saturn and Titan (e.g., Jackman et al., 2014; Jasinski et al., 2016; Martin et al., 2020), Uranus (DiBraccio and Gershman, 2019, who also note a lack of observations of Neptunian flux ropes so far), as well as near comets (Edberg et al., 2016). Flux ropes have also been assumed to form in astrophysical contexts such as black hole accretion disks (e.g., Ripperda et al., 2022). Flux ropes are therefore quite a fundamental and universal phenomenon

35 in magnetised space plasmas.

As noted above, depending on the context flux ropes may be called flux transfer events when considering magnetopause reconnection, or plasmoids in magnetotail or other planetary contexts. Some authors distinguish flux ropes with a strong axial field from plasmoids without axial field, thus with a more cylindrical rather than helical geometry, which can form under very symmetric conditions. In the case of two-dimensional simulations, the term 'magnetic island' is sometimes encountered (e.g.,

40 Fermo et al., 2012; McGregor et al., 2013; Zhou et al., 2014; Pfau-Kempf et al., 2016; Hoilijoki et al., 2019). In this work we use the term 'flux rope' to cover all such rolled-up magnetic field structures forming as part of magnetic reconnection.

Considering in situ observational data, the classical signature of a flux rope passing by the spacecraft is a bipolar oscillation of the magnetic field component B_N normal to both the axis of the flux rope and the direction of propagation of the flux rope. It is usually seen in the time series of magnetic field components, optionally after transforming into a coordinate system

45 maximising the variance of the oscillating component. If the spacecraft does not cross close to the axis yet there is the suspicion of a passing flux rope nearby, assumptions can be made about the properties of the flux rope and a fit to a model equation can be made to solve for flux rope orientation and size. This is the principle of the Grad-Shafranov reconstruction or more recent methods (see, e.g., Isavnin et al., 2011, for a review). A further example is the method developed by Huang et al. (2018) to detect FTEs by correlating observed magnetic field signatures with a characteristic 'target function to be correlated' built

50 upon an idealised, cylindrical flux rope configuration. This is essentially a refinement of the identification of the bipolar B_N signature.

When considering simulation data analysis, ad hoc tracing of field lines is commonly used to show the existence of flux ropes. Paul et al. (2022) developed an automated method to detect and track FTEs in their global magnetospheric simulation output. They first identify FTEs by inspecting B_N signatures on the magnetopause. They then use an algorithm that builds

55 a tree representation of the data cube of thermal pressure in one simulation snapshot. Each local thermal pressure maximum and the surrounding volume are assigned an index that allows tracking in consecutive simulation snapshots. The obtained

dendrogram is then 'pruned to get rid of other high-pressure regions in the domain that are not of interest' and identified high-pressure structures are matched to the FTEs. This method thus allows to assign a connected simulation volume characterised by a thermal pressure signature to a given FTE.

60   In the context of remote-sensing data such as the observation of flux ropes at the Sun's surface, in the corona and beyond, techniques have been developed taking advantage of magnetograms of the solar surface as well as optical observations (e.g., Isavnin et al., 2014; Liu, 2020; Wagner et al., 2024). Derived methods can be applied to detect flux ropes in simulations of the Sun's surface and corona. For example Lowder and Yeates (2017) calculate the magnetic field lines' helicity and the twisted magnetic field of flux ropes is characterised by high helicity, peaking at the centre of the flux rope. This is used to define
65   thresholds that allow to define the flux rope footpoints in the photosphere and the volume of the flux ropes over the surface.

In this work, we introduce a new method to detect flux ropes in a general way in global simulations, without prior assumptions about their shape, orientation, or location near current sheets or other pre-determined structures of interest (Section 2). Our method can be applied to any magnetised plasma simulation setup in principle, and it is used in this work to detect and follow flux ropes comprehensively in a global, three-dimensional simulation of the Earth's magnetosphere performed with
70   the hybrid-Vlasov model Vlasiator (Palmroth et al., 2018; Ganse et al., 2023; Pfau-Kempf et al., 2024). The implementation is discussed in Section 2.2 and the global simulation setup is presented in Section 3. The results are presented in Section 4, allowing to characterise the output of the proposed flux rope identification algorithm and to track flux ropes comprehensively throughout the simulation run. In particular, the propagation of FTEs from the dayside to the far magnetotail flanks is studied. A discussion of the obtained results and the flux rope detection algorithm's parameters is given in Section 5 and we present our
75   conclusions in Section 6.

2   Flux rope identification algorithm

2.1   Method

The impetus for developing a new algorithm to detect flux ropes in a magnetospheric simulation comes from several reali-sations. Firstly, in simulations, flux ropes such as FTEs forming at and propagating along the magnetopause, or plasmoids
80   forming in magnetotail reconnection, can exhibit cross-sections ranging from the numerical grid scale at formation to several Earth radii ($1\,R_{\mathrm{E}} = 6371\,\mathrm{km}$). Secondly, their orientation can be arbitrary. Thirdly, the method should be independent from having to first identify interfaces such as the magnetopause or tail current sheets so as to identify flux ropes anywhere in the simulation volume. This leads to the requirements that the method should not rely on 1) arbitrary length scales such as a fixed absolute search radius or field line tracing length, 2) specific directions or coordinates, nor 3) prior identification of features
85   like current sheets or processes like magnetic reconnection. Furthermore, the variety of scales leads to the conclusion that a local method using only variables and their derivatives defined at a given simulation point is not sufficient to capture large and potentially complex flux rope configurations. This is discussed in more detail in Section 5.2.

Since the most general feature of flux ropes is the twisting of their magnetic field $\boldsymbol{B}$, the algorithm is designed to determine where magnetic field lines are tightly wound. This is done by tracing the magnetic field backward and forward from every

Annales
Geophysicae
Discussions
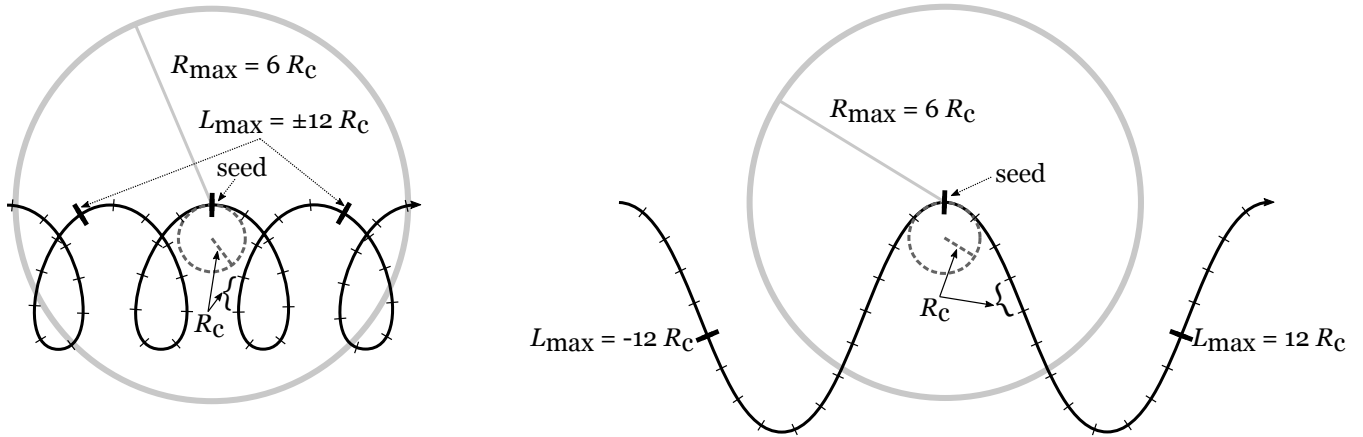
Figure 1. Illustration of the flux rope identification method for the parameters $L_{\mathrm{max}} = 12\,R_{\mathrm{c}}$ and $R_{\mathrm{max}} = 6\,R_{\mathrm{c}}$. Magnetic field lines are black. (a) The magnetic field is sufficiently twisted, when tracing the field for a length of L_{max} in either direction the radius R_{max} is not exceeded. This seed point is thus part of a flux rope. (b) The magnetic field is not very twisted, when tracing the field for a length of L_{max} in either direction the radius R_{max} is exceeded. This seed point is not part of a flux rope.

numerical grid point in the simulation up to a maximum tracing distance along the field line L_{max}. If both the forward and backward parts of the field line did not exit a sphere with a radius of R_{max} centred on the seed point, the seed point is considered to be part of a flux rope. L_{max} and R_{max} are expressed in units of the curvature radius $R_{\mathrm{c}} = 1/|\boldsymbol{b} \cdot \nabla \boldsymbol{b}|$ (where $\boldsymbol{b} = \boldsymbol{B}/|\boldsymbol{B}|$), in order for the algorithm to adapt to the local scale of magnetic field structures. This method is illustrated in a cartoon fashion in Figure 1.

2.2 Implementation

The algorithm described above is implemented and optimised for runtime execution during full three-dimensional simulations of the Earth's magnetosphere using the hybrid-Vlasov model Vlasiator (Palmroth et al., 2018; Pfau-Kempf et al., 2024). Magnetic field tracing is performed using a simple, adaptive Euler algorithm (e.g., Press et al., 2011), limited to step lengths ranging 100–1000 km or 0.1–1 times the highest-resolution numerical grid cells used in magnetospheric simulation setups (see Section 3). The magnetic field is split into a static, curl-free background component and a propagated, perturbed component (von Alfthan et al., 2014; Palmroth et al., 2018). All variables related to the field solver are stored on a uniform, Cartesian grid at the finest resolution, and tracing is performed on this grid (Papadakis et al., 2022). During tracing, the background field components are obtained at arbitrary coordinates (x, y, z) using the same analytic expressions that are used to set them at initialisation. The perturbed components are reconstructed to second order at the same coordinates (x, y, z) using the formalism by Balsara (2009) used in Vlasiator's field solver as well (Palmroth et al., 2018). Reconstructing the field at any (x, y, z) during tracing yields more accurate results than only using the components stored at grid locations. The reconstruction requires a comprehensive set of derivative values to be available. Storing them all in order to perform the tracing post hoc would require

tens of gigabytes of disk space per output file corresponding to a given time in the simulation, which is prohibitive. Hence the decision was made to perform this algorithm as part of in-situ data analysis, that is at runtime.

110   The seed points (x_0, y_0, z_0) for tracing are taken as the centres of the cells of the spatially refined mesh which is used to store and propagate the plasma's velocity distribution function (Papadakis et al., 2022; Ganse et al., 2023; Kotipalo et al., 2024). At each seed point, the curvature radius R_c is determined. Then tracing is performed along $\pm \boldsymbol{B}$, recording the maximum extent $R^{\pm} = \max\left(|(x_0, y_0, z_0) - (x_n, y_n, z_n)|\right)$ over all successive n tracing steps, until the tracing reaches the distance $L_{\max}$ along the field line. If both $R^+ < R_{\max}$ and $R^- < R_{\max}$ (like in Figure 1(a)), the value of $R_{\mathrm{cutoff}} = \max(R^+, R^-)$ is recorded for

115   the location (x_0, y_0, z_0). If $R^+ > R_{\max}$ or $R^- > R_{\max}$ (like in Figure 1(b)), if a boundary of the domain is reached, or if tracing reaches values of $R^{\pm}$ significantly larger than the domain size, tracing is stopped (see Section 2.3). For the particular simulation run presented in this work, $L_{\max} = 12\,R_c \approx 4\pi\,R_c$, hence tracing is allowed to proceed up to almost two turns around an ideal, cylindrical configuration of radius R_c. The maximum extent is set to $R_{\max} = 10\,R_c$, thus values of R_{cutoff} in the range 0–10 are stored for each seed point, allowing for later determination of a suitable threshold to be used for analysis

120   (see Section 4.2).

2.3   Termination conditions

The flux rope detection algorithm is executed during large-scale simulation runs performed on tens of thousands of supercomputer cores. The simulation volume is decomposed into thousands of spatial domains mapped to individual computational tasks using the Message-Passing Interface (MPI). Field lines are traced from every grid cell through potentially large swathes of the

125   simulation volume. The implementation of the algorithm was optimised in terms of memory and inter-task communications in the context of the specific grid libraries and data structures used by the code. Further optimisations informed by the nature of the physical problem at hand are critical to avoid spending a large fraction of the computation time on this analysis. They are described here.

Other data products generated at runtime include tracing the magnetic field in the whole domain to obtain connection

130   information, allowing to determine the open and closed field regions. The flux rope detection is performed alongside the full-domain tracing, avoiding tracing the same field lines twice. That tracing naturally includes termination conditions at the inner and outer boundaries.

Due to the inaccuracy inherent to the discretisation of the problem, and especially in regions of tightly-wound field configurations near the numerical grid resolution, it is possible that the field line tracing circles around certain regions for long

135   distances without ever exiting the domain. Furthermore, during prototyping of the algorithm a peculiar structure was identified in the initialisation phase of the magnetospheric setup. When the magnetotail forms, a pair of magnetic field line loops forms at either edge of the tail current sheet, near the transition between the tail current sheet and the magnetosheath. These field lines stretch for tens of R_E along the tailward flow, that is the x-direction, turning around at the tips of this long and thin structure. In the y- and z-direction this structure is only a few R_E in size. In the middle of this structure, R_c is much larger than the

140   simulation domain, leading to a very large $L_{\max}$. While algorithmically correct, the detection of this type of structure is not relevant in the context of magnetospheric simulations, where flux ropes are considered to be bundles of magnetic flux winding

around their axial direction. Therefore, a termination condition interrupts the field line tracing if the traced distance $L^{\pm}$ reaches a limit. The limit defaults to the sum of the simulation domain size in every coordinate direction but it can also be set ad hoc by the user.

145   Finally, both the full-domain tracing and the flux-rope detection feature a parameter allowing to leave a fraction of cells unresolved. Once that limit is reached, the algorithm stops, providing another way to tune its computational cost.

3   Global magnetospheric simulation setup

Vlasiator is a hybrid-Vlasov simulation code modelling ions (only protons herein) using their discretised velocity distribution function while electrons are a charge-neutralising fluid. It is mainly tailored towards large-scale simulations of the terrestrial

150   magnetosphere and its surrounding magnetosheath–bow shock–foreshock system (von Alfthan et al., 2014; Palmroth et al., 2018). The code is openly available under the GNU GPL-2 license (Pfau-Kempf et al., 2024) and the model is typically run on hundreds of nodes on top-tier supercomputers due to the large memory and computational requirements (Ganse et al., 2023; Kotipalo et al., 2024).

In this work, we present a simulation run in a volume spanning $[-110; 50]\,R_\mathrm{E}$ in the x-direction and $[-58; 58]\,R_\mathrm{E}$ in the

155   y- and z-directions of the Geocentric Solar-Magnetospheric (GSM) coordinate system. The base grid of $128 \times 92 \times 92$ cells yields a coarsest spatial resolution of $\Delta x = 8000\,\mathrm{km} = 1.26\,R_\mathrm{E}$ and it is statically refined up to three levels, yielding a finest spatial resolution of $\Delta x = 1000\,\mathrm{km} = 0.16\,R_\mathrm{E}$ in the tail current sheet and at the dayside magnetopause (Papadakis et al., 2022; Ganse et al., 2023; Kotipalo et al., 2024). The velocity space resolution is $\Delta v = 40\,\mathrm{km\,s^{-1}}$. The phase-space density threshold, below which the velocity distribution is neither stored nor propagated (von Alfthan et al., 2014; Palmroth et al.,

160   2018), is set to $10^{-15}\,\mathrm{m^{-6}s^3}$ where the proton number density is higher than $10^5\,\mathrm{m^{-3}}$, to $10^{-17}\,\mathrm{m^{-6}s^3}$ where the proton number density is lower than $10^4\,\mathrm{m^{-3}}$, and linearly interpolated in between. The $+x$ inflow wall maintains constant inflow and interplanetary magnetic field (IMF), the other walls maintain Neumann (copy) conditions ensuring outflow of plasma. The spherical inner boundary is centred around the origin of the simulation domain where the Earth is located and it is set at a radius of $4.7\,R_\mathrm{E}$. It couples the hybrid-Vlasov domain with an ionospheric model solving for the ionospheric potential using a

165   height-integrated conductivity model (Ganse et al., 2024). Field-aligned currents computed near the inner boundary are mapped along the magnetic field to the ionospheric grid. Using parameterised particle precipitation and a model atmospheric profile from the NRLMSISE model (Picone et al., 2002), ionisation rates and thus conductivities are computed and height-integrated, so that the electric potential can be solved for on the ionospheric grid. The gradient of the electric potential is mapped back into the hybrid-Vlasov domain and used to determine an electric field $\boldsymbol{E}$ and hence an $\boldsymbol{E} \times \boldsymbol{B}$ drift velocity that is given to the

170   ion velocity distribution functions near the inner boundary.

The initial and inflow solar wind conditions are uniform and steady with a proton number density of $10^6\,\mathrm{m^{-3}}$, a temperature of $0.5\,\mathrm{MK}$ and a velocity of $(-750, 0, 0)\,\mathrm{km\,s^{-1}}$. For the initial simulation state, inside a radius of $15.7\,R_\mathrm{E}$, the velocity is gradually tapering from the solar wind velocity to zero at the inner boundary. The initial magnetic field is the unscaled,

Annales
Geophysicae
Discussions

unperturbed geomagnetic dipole with 0° tilt angle, gradually transitioning to the constant IMF of $(0, 0, -5)\,\mathrm{nT}$ towards the
175    $+x$-direction.

4   Results

With its fast solar wind and moderate, purely southward IMF, the simulated setup produces active dayside reconnection. This
generates FTEs as previously studied in 2D (Pfau-Kempf et al., 2016; Jarvinen et al., 2018; Hoilijoki et al., 2019; Akhavan-
Tafti et al., 2020; Pfau-Kempf et al., 2020; Grandin et al., 2020; Ala-Lahti et al., 2022) and 3D (Pfau-Kempf et al., 2020;
180   Tesema et al., 2024; Grandin et al., 2024), which loads the magnetotail lobes and leads to reconnection of the tail current sheet.
That in turn generates plasmoids and flux ropes as studied previously in 2D (Palmroth et al., 2017; Runov et al., 2021) and in
3D (Palmroth et al., 2023; Grandin et al., 2023). In Sections 4.1 and 4.2 we first illustrate how the method detects flux ropes
throughout the simulation domain and how the outcome is affected by the choice of R_{cutoff}. Sections 4.3 and 4.4 focus on
describing the evolution of FTEs along the dayside and nightside magnetopause, respectively.

4.1   Global mapping of flux ropes in the magnetosphere

Figure 2 illustrates how flux ropes can be mapped in the magnetospheric simulation domain. The view is from the solar wind's
direction towards Earth, that is parallel to the $-x$-direction. The grey surface of the region with closed field lines gives a proxy
for the position of the dayside magnetopause. The algorithm described in Section 2 yields values of 0 when no flux rope is
detected, and non-zero values up to R_{max} in case of detection. Points of detection up to R_{cutoff} values of 3, 5, and 7 are shown
190   in panels (a), (b), and (c), respectively, as spherical markers. To confirm the nature of the detections, magnetic field line stubs
forward and backward from each detection point are plotted too. They are capped at a field line length of $L_{\mathrm{max}} = 12R_{\mathrm{c}}$ from
the detection point. The colour of the spheres and lines shows the curvature radius at the seed point, given in units of R_{E}.
Figure 3 shows the same plotted information as viewed from North along the $-z$-direction.

In both Figures 2 and 3 it is clear that structures with curvature radii of the order of $R_{\mathrm{c}} \approx 6\,R_{\mathrm{E}}$, coloured purple, are
195   inconsistent with the scale of flux transfer events on the dayside magnetopause, which itself has a curvature of a similar order
of magnitude. In the same way in Figure 3 some structures with high R_{c} at the detection point are visible in the magnetotail.
These detections are the result of the large curvature radius at the starting point, leading to the field line stretching out for tens
of R_{E} but still less than R_{max}. It can thus be useful to filter out curvature radii too large compared to the scale of the system
under consideration, such as the magnetopause, but they are retained here for illustration purposes.

4.2   Sensitivity of R_{cutoff}

Given that a single production-scale run with Vlasiator costs tens of millions of core-hours on modern supercomputers, the
value of $R_{\mathrm{max}} = 10\,R_{\mathrm{c}}$ was chosen conservatively high. Figures 2 and 3 illustrate the effect of setting R_{cutoff} to the values of
3, 5, and 7 R_{c} (panels (a), (b), and (c), respectively).
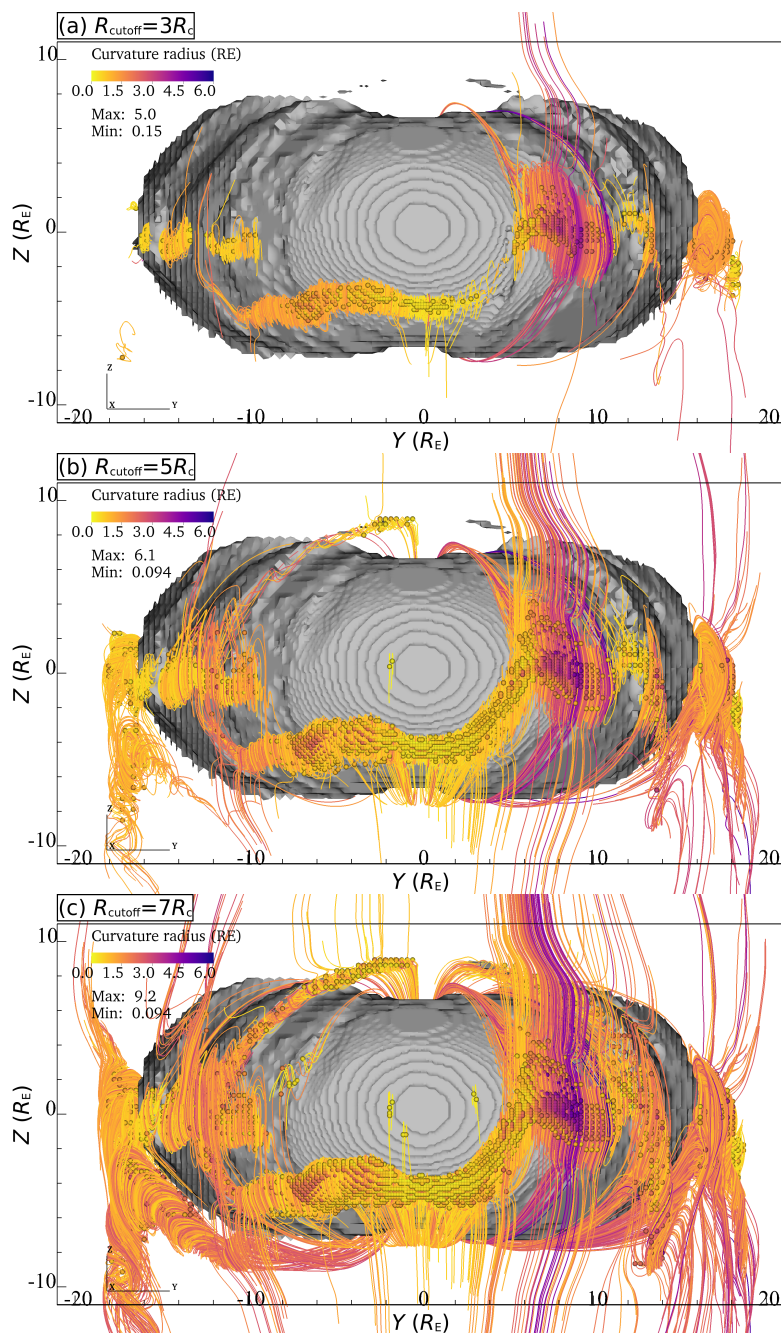
Figure 2. Flux ropes detected in the simulation at t=1600 s. View of the dayside from the direction of the solar wind, axes (GSM coordinates) in R_E. Grey: surface of the region of closed magnetic field lines connected at both ends to the inner boundary. Spheres: points near flux ropes detected by the algorithm. Lines: magnetic field lines traced from the detected points out to R_{cutoff}. Colour scale: curvature radius R_c at detection point, in units of R_E. Panels (a)–(c): $R_{cutoff} = 3, 5, 7\,R_c$.
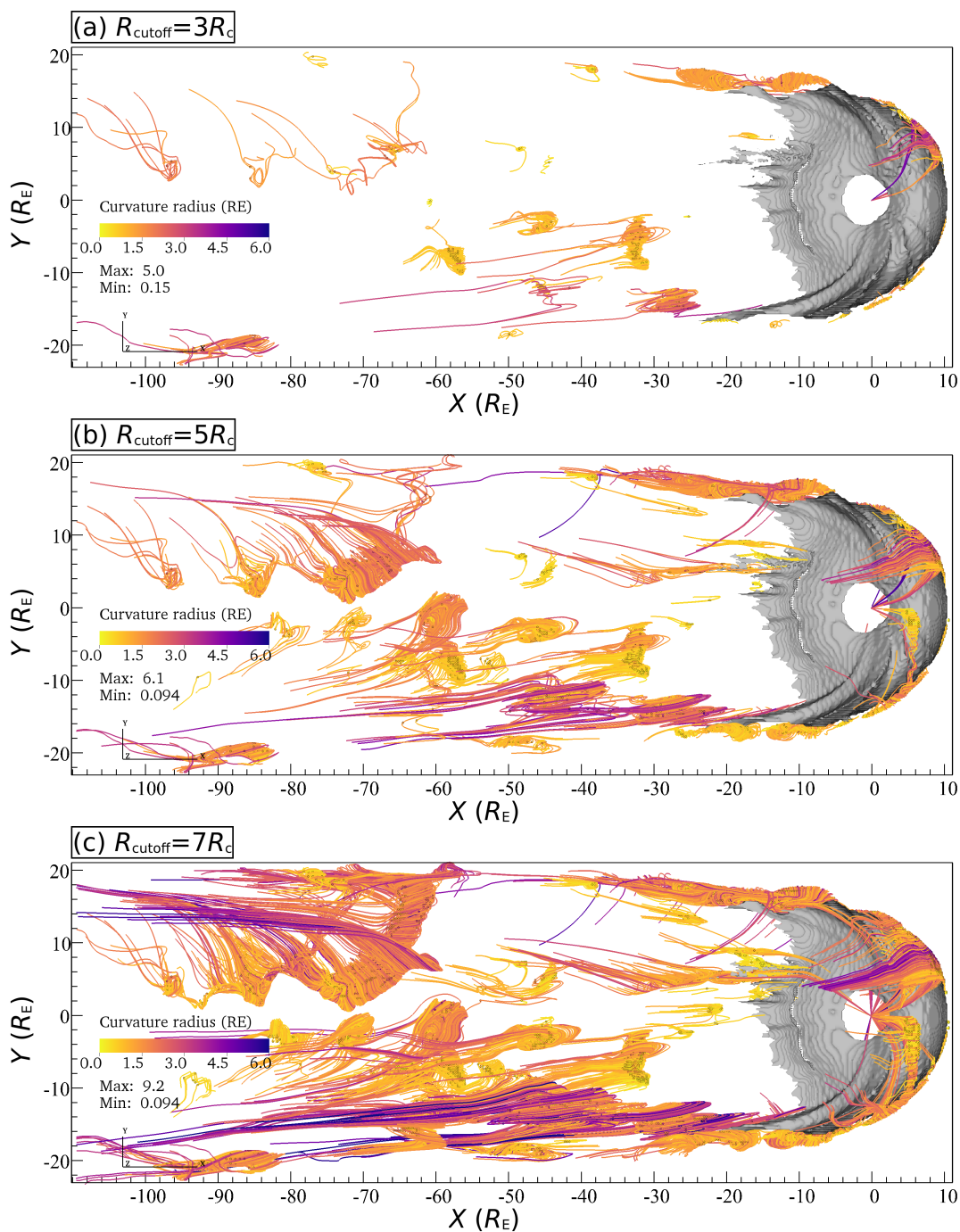
Figure 3. Same format as Figure 2, view from above the equatorial plane, showing wound-up magnetotail structures.

Comparing the panels in Figure 2, it is clear that too low an R_{cutoff} value can lead to failing to register flux ropes that are
205 detected at higher values. Two prominent examples are the long flux rope in the $(-y, +z)$-quadrant and the curved flux rope in
the $(-y, -z)$-quadrant, which are absent in panel 2(a) at $R_{\mathrm{cutoff}} = 3\,R_{\mathrm{c}}$, partially detected in panel 2(b) at $R_{\mathrm{cutoff}} = 5\,R_{\mathrm{c}}$ but
well covered in panel 2(c) at $R_{\mathrm{cutoff}} = 7\,R_{\mathrm{c}}$. The same behaviour can be identified by comparing the flux ropes detected at the
various levels of R_{cutoff} in the magnetotail as shown in Figure 3.

At even higher values of R_{cutoff} (not shown), especially for large curvature radii, the algorithm detects structures that
210 fulfil the field line extent criterion but are not rolled up into flux ropes. They are generally bent field structures such as the
magnetopause or tail current sheets.

The analysis of flux ropes therefore requires a careful choice of R_{cutoff}. It has to be low enough to minimise the amount of
false positives on the one hand, and high enough to detect also the more loosely wound structures on the other hand. Motivated
by this analysis, a value of $R_{\mathrm{cutoff}} = 7\,R_{\mathrm{c}}$ is chosen for rest of this work.

215 ### 4.3   Evolution of FTEs on the dayside

Under southward IMF conditions as in the simulation used in the present work, reconnection occurs at low latitudes on the
dayside magnetopause (e.g., Trattner et al., 2021). Owing to the spatial and temporal variability of magnetic reconnection,
FTEs form and are pushed along the magnetopause by the reconnection exhausts as well as the ambient magnetosheath plasma
flow. We first investigate the evolution of the FTEs produced under these conditions in the subsolar region of the dayside
220 magnetopause.

In Figure 4, the panels 4(a)–4(d) show the North-South velocity component V_z in the $x - z$ plane at coordinates $y = -4.5, -1.5, 1.5, 4.5\,R_{\mathrm{E}}$ in colour, with the thin black magnetic field line stubs illustrating the general magnetic topology.
As a further guide, the magnetopause is detected with the modified plasma β parameter which includes the dynamic pressure,
$\beta^* = 0.5$ (Xu et al., 2016; Brenner et al., 2021), and shown as a thick black contour. The purple X and yellow square mark-
225 ers denote X- and O-points, respectively, as detected with the method of Alho et al. (2024) based on the minimum gradient
analysis (MGA) and minimum directional derivative (MDD) techniques. The regions detected as being near flux ropes at the
level of $R_{\mathrm{cutoff}} = 7\,R_{\mathrm{c}}$ are marked in green. Naturally, detected flux ropes (green circles) are coinciding with O-points (yellow
squares). The panels 4(e)–(f) show the latitude – magnetic local time (MLT) map of the open-closed magnetic field boundary
(OCB) as a black contour in the North and South ionosphere (set at an altitude of $100\,\mathrm{km}$, as explained by Ganse et al., 2024),
230 respectively. Additionally, the footpoints of flux ropes magnetically connected to the ionosphere are plotted on these maps as
well. They are marked with a circle if the source point in the flux rope is at a coordinate $|y| < 4.5\,R_{\mathrm{E}}$ encompassed by the
planes of panels (a)–(d), and a + marker otherwise. The footpoints are coloured according to the (x, z)-coordinate of their
source point, following the two-dimensional colour map shown. This Figure 4 is a snapshot at simulation time $t = 1612\,\mathrm{s}$ from
Supplementary Material Animation 1, which covers the time interval 1073–1612 s.

235 At numerous times and locations along the magnetopause, strong exhaust channels visible in V_z on either side of X-lines
confirm the occurrence of active reconnection, in a patchy and bursty fashion as investigated previously (Pfau-Kempf et al.,
2020). A prominent reconnection exhaust channel can be seen for example in Figure 4(a)–(d) northward of the X-line at
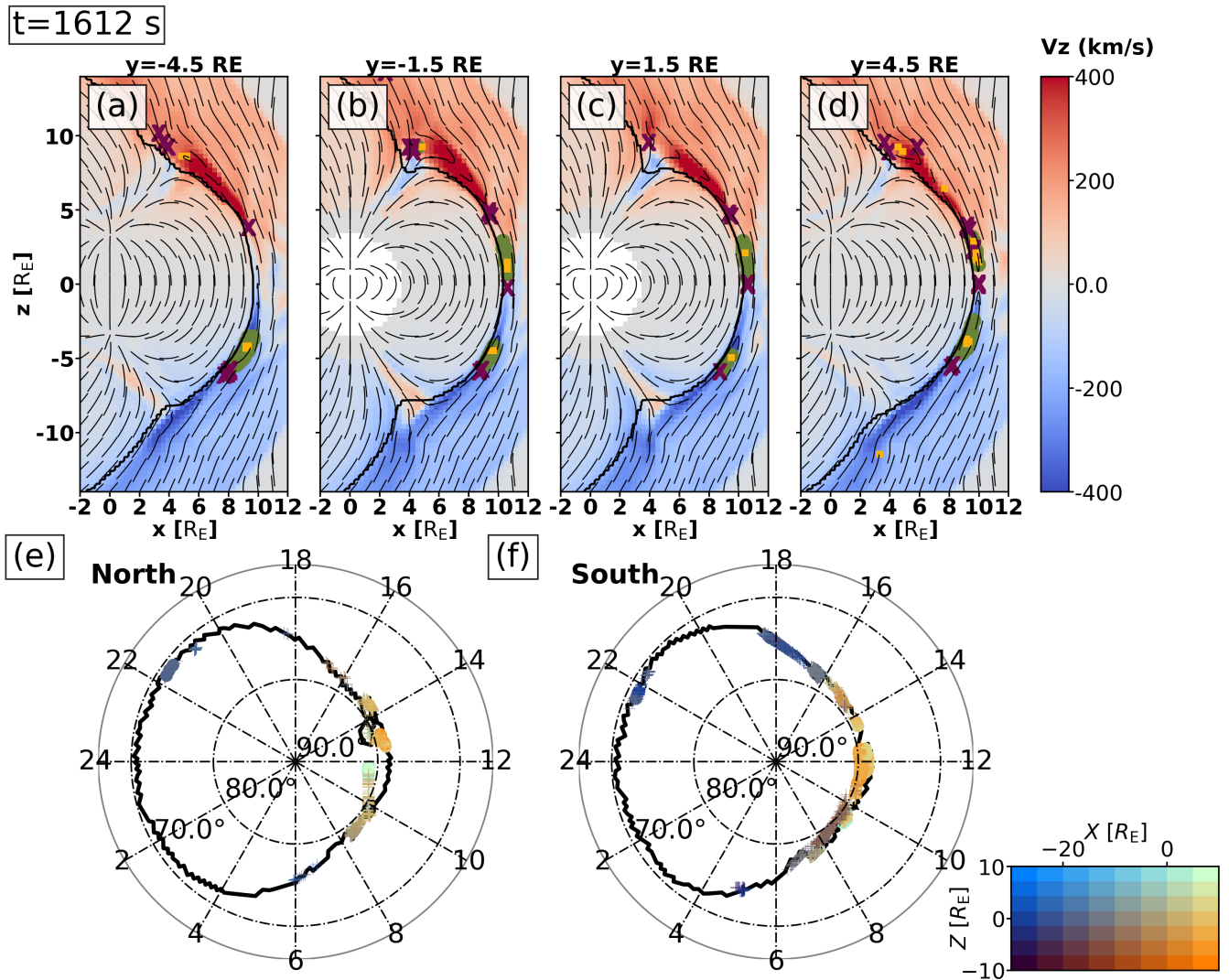
Figure 4. Panels (a)–(d): North-South velocity component V_z (colour) in the (x, z)-plane at coordinates $y = -4.5, -1.5, 1.5, 4.5\,R_{\mathrm{E}}$. The thin black lines are tangent to the magnetic field. The thick black contour is set at $\beta^* = 0.5$ (Xu et al., 2016; Brenner et al., 2021) to show the magnetopause position. The purple X and yellow square markers denote X- and O-lines using the Alho et al. (2024) method. The green circles denote the regions where flux ropes are detected at the level of $R_{\mathrm{cutoff}} = 7\,R_{\mathrm{c}}$. Panels (e)–(f): North and South hemisphere ionospheric latitude – magnetic local time (MLT) map of the open-closed magnetic field boundary (black contour). The footpoints of detected flux ropes are marked with a circle if the source point in the flux rope is at a coordinate $|y| < 4.5\,R_{\mathrm{E}}$, and a + marker otherwise. The footpoints are coloured according to the (x, z)-coordinates of their source point, following the two-dimensional colour map shown. This figure is at $t = 1612\,\mathrm{s}$ from the beginning of the simulation. See the animated version of this figure for the time interval 1073–1612 s as Supplementary Material Animation 1.

$z = 4\,R_{\mathrm{E}}$. Many more FTEs are seen in Supplementary Material Animation 1 forming at lower $|z|$ and moving along the diverging magnetosheath flow northwards and southwards of the equatorial plane ($z = 0$).

240   Once the FTEs have reached the tailward portion of the cusp, their leading side comprises a magnetic field component antiparallel to the magnetic field of the magnetosphere, thus conducive to magnetic reconnection. At $t = 1612\,\mathrm{s}$ in Figure 4(a)–4(d), active reconnection is seen near $(x = 4\,R_{\mathrm{E}}, z = 9\,R_{\mathrm{E}})$. The remnants of the FTE are still denoted by the yellow squares and green circles, and an X-line is seen on the leading side. Enhanced flows are evidence of active reconnection exhaust channels, into the cusp (blue enhancement in panels 4(b) and 4(c)) as well as outwards (red enhancement northward of the X-

245 line in panel 4(c) in particular). Further clear examples of magnetic reconnection can be identified in Supplementary Material Animation 1 for example at the North cusp during the approximate times 1430–1450, 1530 and 1612 s. Some aspects of this FTE-cusp reconnection process have been studied using a magnetohydrodynamic model by Paul et al. (2023).

     By definition, magnetic reconnection modifies the topological configuration of spatially adjacent magnetic domains and FTEs carry away newly-opened flux from the magnetosphere. It is thus expected to see signatures of FTEs in the OCB plotted

250 in Supplementary Material Animation 1 and Figure 4(e)–4(f). As a baseline, it can be observed that during the period of about 1150–1220 s, the OCB is mostly smooth and convex on the dayside in the absence of large FTEs perturbing the magnetopause. A number of FTEs form after 1200 s, their footpoints straddling the OCB, but they do not modify the position of the OCB significantly. The fine-scale jaggedness of the OCB is due to the triangular tessellation of the Fibonacci grid used for the ionosphere solver (Ganse et al., 2024). During the time interval 1350–1450 s, large FTEs travel both North and South towards

255 higher latitudes on the magnetopause, and they indent the OCB mostly between 9 and 15 MLT. A period with clearly identified indentations of the OCB is around 1415 s, when the OCB is indented at 11–14 MLT in the North and at 9–13 MLT in the South. Similar perturbations of the OCB are registered again from 1570 s to the end of the simulation, as is also visible in Figure 4(e)–4(f). The footpoints show that the highest-latitude FTEs are connected the deepest in the open field region, poleward of the OCB in the dayside region, and the footpoints vanish at the same time as their source FTEs vanish through reconnection in the

260 cusps.

4.4   Evolution of FTE flux ropes on the nightside

Inspecting the outcome of the flux rope detection method with plots like Figure 3 and animations thereof (not shown) reveals that flux ropes are not limited to the dayside as presented in Section 4.3, nor to the tail current sheet (as studied with Vlasiator by Palmroth et al., 2023; Alho et al., 2024). There is a population of flux ropes forming at low $|z|$ on the dayside which travel

265 with the magnetosheath flow along the flanks of the magnetopause from the dayside to tens of R_{E} downtail on the nightside, as suggested by the detection of flank O-lines by Alho et al. (2024). Indeed Figure 4(e)–(f) as well as Supplementary Animation 1 show a significant population of flux rope footpoints that are connected to the morning or evening sector of the OCB. They are mostly denoted with + markers as their source flux rope is beyond the span of the plotted planes of panels 4(a)–(d), that is at $|y| > 4.5\,R_{\mathrm{E}}$. Furthermore, their colour indicates that they exist at low $|z|$, meaning they exist near the equatorial region

270 of the magnetopause. They lose their connection to the ionosphere eventually, as the footpoints are seen to disappear, but the flux ropes do not cease to exist, as shown in the following. A third population of flux rope footpoints can be discerned in

Figure 4(e)–(f) and Supplementary Animation 1 in the 21–3 MLT night sector. They are the signatures of plasmoids forming in magnetotail current sheet reconnection processes, as studied previously (Palmroth et al., 2023; Alho et al., 2024). Those will be the subject of separate studies and are thus left out of the scope of this work.

275   Figure 5 and its animated version Supplementary Material Animation 2 present a flux rope which is still relatively close to Earth around $x = -10\,R_{\mathrm{E}}$. It is the curved flux rope that is also visible in the $(-y, -z)$-quadrant of Figure 2(c). The morphology of the flux rope is described by the spatial cuts through the flux rope of panels 5(a) and 5(b) in two orthogonal planes. The in-plane components of the magnetic field are shown with the black tangent lines whereas the colour in the background shows the out-of-plane component. The green contour delimits the region of flux rope detection at the level of $R_{\mathrm{cutoff}} = 7\,R_{\mathrm{c}}$. This

280   flux rope is very curved, as evidenced by panel 5(b), as well as the pair of counter-rotating vortices of magnetic field lines at $y = -17\,R_{\mathrm{E}}$; $z = -6\,R_{\mathrm{E}}$ and $-7.5\,R_{\mathrm{E}}$ in panel 5(a). It passes over a string of four virtual spacecraft locations marked in panels 5(a)–5(b) and the magnetic field time series at these locations are shown in panels 5(c)–5(f). We do not proceed to a change of coordinate system to allow for direct comparison of the slices in panels 5(a)–5(b) with the virtual spacecraft time series. Due to the curved shape of the flux rope, the characteristic bipolar signature of the passing flux rope is not readily

285   observed in a single magnetic field component. However it is detected by the two lower virtual spacecraft (panels 5(e)–5(f)) during the time interval 1560–1580 s. They cross the leading portion of the flux rope, which despite its curvature has an axial orientation approximately along the z-direction, that is perpendicular to the tailward magnetosheath flow in the $-x$-direction. At the location of the lowest virtual spacecraft, the axis of the flux rope axis is nearly aligned with the z-direction so that the bipolar oscillations are well visible in the B_x and B_y components of panel 5(f). At the second location (panel 5(e)) the axis of

290   the flux rope is more inclined along the main diagonal of the (x, y)-plane so that the signature is less obvious but can still be inferred in the B_y component. Both these virtual spacecraft also show a clear dip in the magnetic field magnitude B, indicative of their passing near the core of the flux rope where the field is close to zero, as confirmed by the sign flip of the out-of-plane components in panels 5(a) and 5(b). The two upper virtual spacecraft of panels 5(c) and 5(d) on the other hand are observing the trailing part of this flux rope, whose axis is much more aligned with the ambient flow direction, making it geometrically

295   impossible to observe a bipolar signature or the magnetic field magnitude approaching zero.

    Figure 6 tracks the propagation of a flux rope whose longitudinal axis is essentially parallel to the flow and the x-direction. Each pair of consecutive panels is in the same format as panels (a)–(b) of Figure 5, showcasing the three-dimensional structure of the flux rope. Its rolled-up magnetic field is clearly visible as a vortex of the black lines in panels 6(a), 6(c), 6(e), and 6(g) encompassed by the green contour, and the elongated structure parallel to the x-direction is clearly visible in panels 6(b),

300   6(d), 6(f), and 6(h) in both the colour plot and the green contour. A further guide to the location of this flux rope is given by the large-scale patterns in the out-of-plane B_x in the left panels 6(a), 6(c), 6(e), and 6(g): the bipolar sign change of B_x at $x \gtrsim -17\,R_{\mathrm{E}}$; $z \approx 0$ corresponds to the centre of the magnetotail current sheet separating the North and South magnetotail lobes. Furthermore, the transition from mostly southward field to less homogeneous orientations near $y = -20\,R_{\mathrm{E}}$ ($-18\,R_{\mathrm{E}}$ in panel 6(a)) corresponds to the magnetopause. Over the course of 300 s, this flux rope keeps its characteristic shape and orientation,

305   especially its longitudinal alignment with the magnetosheath flow and the x-direction. However it is seen to gradually shrink, from a diameter of over $2\,R_{\mathrm{E}}$ in panel 6(a) to only about $1\,R_{\mathrm{E}}$ in panel 6(g) in the end, and a length of over $15\,R_{\mathrm{E}}$ initially in
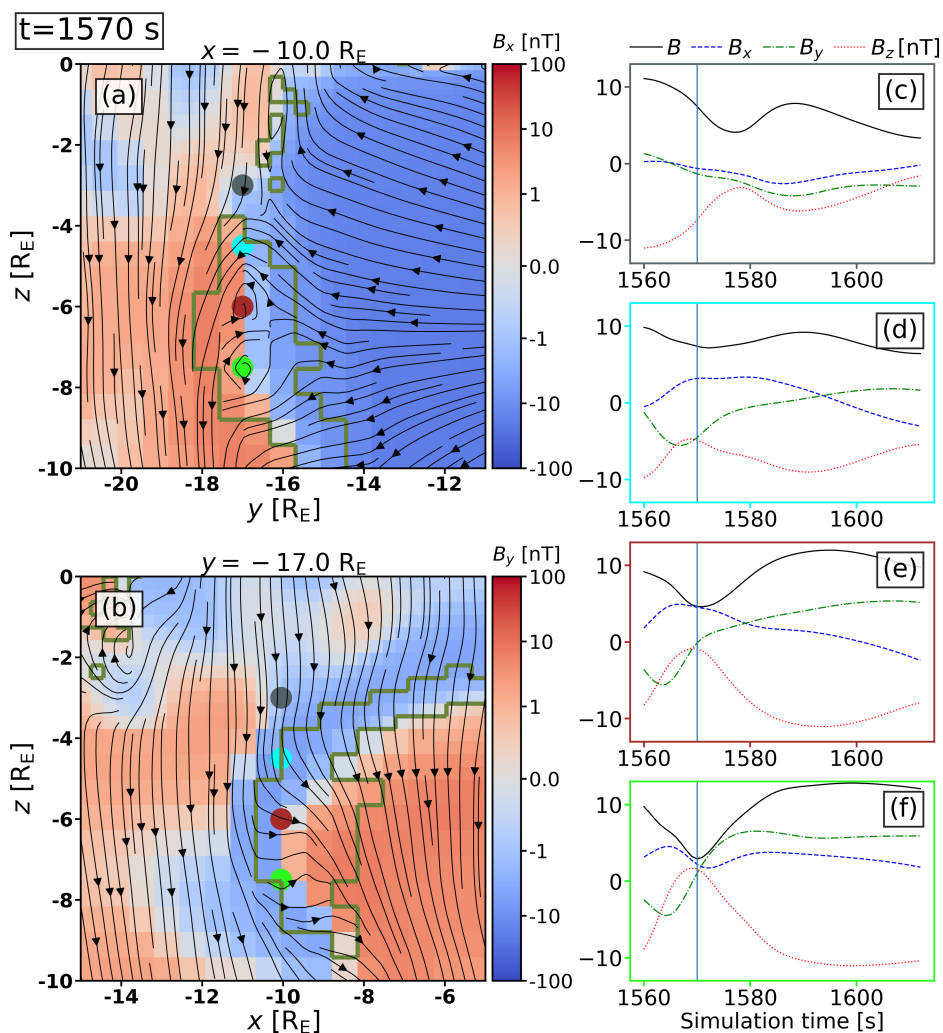
Figure 5. Panels (a) and (b) show a slice through a flank flux rope at time $t = 1570\,\mathrm{s}$ in the (y, z)-plane (resp. (x, z)-plane) at $x = -10\,R_\mathrm{E}$ (resp. $y = -17\,R_\mathrm{E}$). The colour shows the orthogonal B_x (resp. B_y) component of the magnetic field whereas the black lines are tangent to the in-plane magnetic field. The green contour encompasses the regions where flux ropes are detected at the level of $R_\mathrm{cutoff} = 7\,R_\mathrm{c}$. Panels (c)–(f) show the time series of magnetic field magnitude and components for the time interval 1560–1612 s at the four virtual spacecraft locations marked in panels (a)–(b), with the vertical line marking the time of panels (a)–(b). See the animated version of this figure as Supplementary Material Animation 2.

panel 6(b) to about $5\,R_\mathrm{E}$ in panel 6(h). Crucially, at t=1600 s, what remains is a flux rope with a longitudinal axis that is parallel with the x-axis and a magnetic field configuration that has no shearing component with the southern lobe's predominantly $B_x < 0$ magnetic field which it is flowing against. Presumably any parts of the flux rope that were shearing with the lobes have

310   eroded through reconnection and are thus absent at later stages, such as the upstream, upwards-oriented end of the flux rope at $x > -12\,R_\mathrm{E}; z > 0$ which is shearing with the northern lobe's $B_x > 0$ in panel 6(b).

We provide a global overview of where flux ropes occur in the simulation domain in Figure 7. For the same level of $R_\mathrm{cutoff} = 7\,R_\mathrm{c}$ as has been used in Figures 4, 5, and 6, and for the time interval 1073–1612 s at a cadence of 1 s, the occurrence of flux ropes is recorded. This is plotted on a $y - z$ map with contours for consecutive ranges of the simulation domain along the

315   x-direction. As an additional guide, the cross-section of the tail lobes at $x = -10\,R_\mathrm{E}$ at $t =$1612 s is plotted in the background to provide an approximate location of the magnetopause encompassing the magnetotail lobes. The yellow contour for $x \in [4; 12]\,R_\mathrm{E}$ shows that all flux ropes on the subsolar dayside sunward of the cusps, which are therefore FTEs, occur within $|z| < 10\,R_\mathrm{E}$, with a small exception in the North near $y = 2\,R_\mathrm{E}$. This confirms what can be inferred from Supplementary Material Animation 1, which does not show any FTEs propagating significantly further than the cusps. The orange contour

320   for $x \in [0; 4]\,R_\mathrm{E}$ and the contours for all values of $x < 0$ show that no flux ropes occur at $|z| > 10\,R_\mathrm{E}$ in this simulation. The only excursion is seen near $y = -15\,R_\mathrm{E}; z = -11\,R_\mathrm{E}$ in the red and purple contours ($x \in [-70, 0]\,R_\mathrm{E}$) and it corresponds to the leading portion of the flux rope presented above in the $(-y, -z)$-quadrant of Figure 2(c), Figure 5, and Supplementary Material Animation 2. The deeper tailward, the lower in $|z|$ the flux ropes are located in the tail near the magnetopause. The range in z is larger inside the magnetotail, corresponding to plasmoids formed by magnetotail reconnection. Through the influence

325   of various instabilities, the magnetotail current sheet is flapping, leading to significant deviations of its location from $z \approx 0$, as studied by Palmroth et al. (2023) and in further separate studies under preparation. As a consequence, tail plasmoids are detected in a wider range in z. The current sheet is nevertheless approximately centred on $z = 0$ in the absence of a geomagnetic dipole tilt or asymmetric driving conditions. The contour for $x \in [-110; -70]\,R_\mathrm{E}$ exhibits a wider spread in y and z which is due to the fact that in the early phase of the time interval considered, some large-scale magnetic structures, which originated in

330   the initialisation of the magnetosphere in this setup, are still in the process of being flushed out of the simulation domain. For the purpose of this study it was however deemed unnecessary to limit the box to a shorter range in x or make that range vary with time.

5 Discussion

The results presented in Section 4 allow to track the motion of flux ropes from the dayside to the far tail, as discussed in the

335   following Section 5.1. They also give insight into the properties and limitations of the flux rope detection method presented in this work. The method is compared to the X- and O-line detection method by Alho et al. (2024) in Section 5.2, and its behaviour in higher guide field configurations is discussed in Section 5.3.
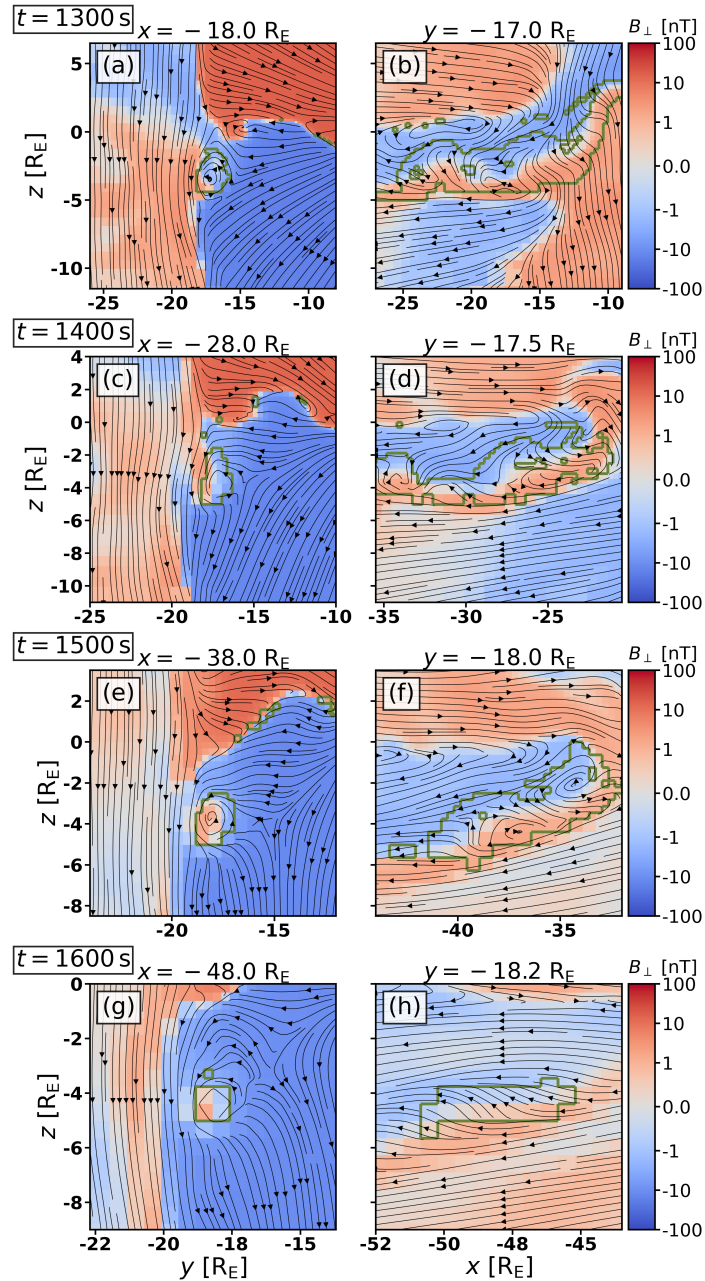
Figure 6. Left column panels (a), (c), (e), and (g) (right column panels (b), (d), (f), and (h), respectively) show slices through a flank flux rope in the (y, z)-plane (resp. (x, z)-plane) at times $t = 1300\,\mathrm{s}$ (panels (a)–(b)), $t = 1400\,\mathrm{s}$ (panels (c)–(d)), $t = 1500\,\mathrm{s}$ (panels (e)–(f)), and $t = 1600\,\mathrm{s}$ (panels (g)–(h)) tracking its tailward propagation. The colour shows the orthogonal B_x (resp. B_y) component of the magnetic field whereas the black stream lines are tangent to the in-plane magnetic field. The green contour encompasses the regions where flux ropes are detected at the level of $R_{\mathrm{cutoff}} = 7\,R_{\mathrm{c}}$.
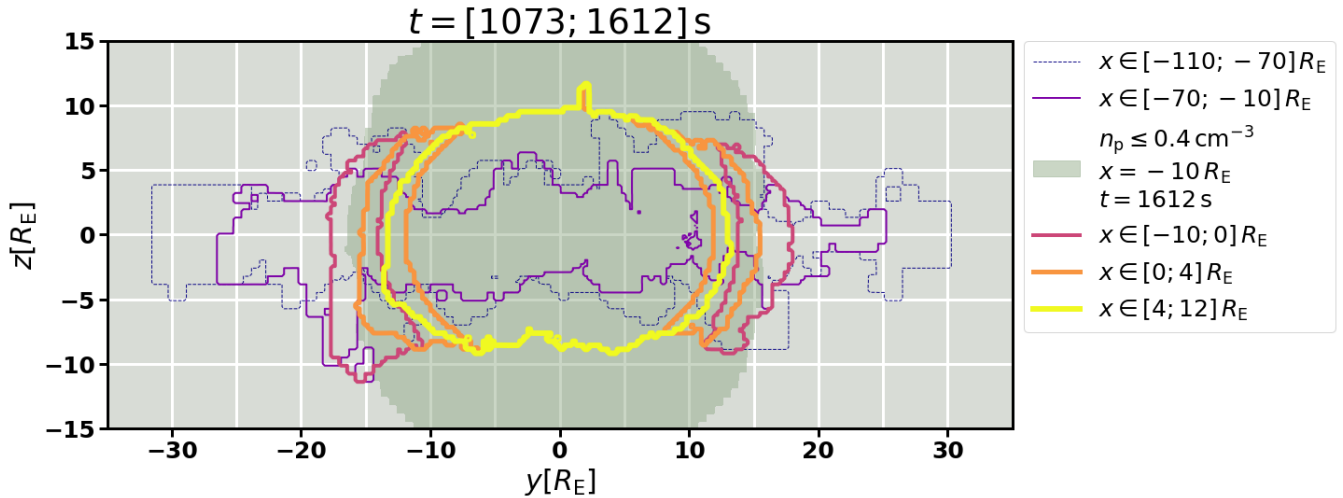
Figure 7. Map of flux rope detection at the level of $R_{\mathrm{cutoff}} = 7\,R_{\mathrm{c}}$, projected onto the (y, z)-plane. Each contour corresponds to a range of the simulation domain in the x-direction and delimits the region where a flux rope is detected at least once for the time interval 1073–1612 s at a cadence of 1 s. The darker shaded region denotes where the ion number density is lower than $0.4\,\mathrm{cm}^{-3}$ at $x = -10\,R_{\mathrm{E}}$ at $t = 1612\,\mathrm{s}$, as a proxy for the location of the magnetopause and tail lobes.

5.1 Global evolution of flux ropes under southward IMF

In the simulation setup presented here (Section 3), namely under purely southward IMF and without geomagnetic dipole tilt,
340 flux ropes form due to magnetic reconnection at the dayside magnetopause near $z = 0$, as shown in Figures 2, 4, and 7 in Section 4. These flux ropes are advected by the local magnetosheath plasma flow, which is globally dominated by the hydrodynamic flow pattern of the shocked solar wind plasma around the magnetopause, but is also locally affected by magnetic reconnection exhausts (e.g., Hoilijoki et al., 2019; Pfau-Kempf et al., 2020). This means that flux ropes can flow into all quadrants of the (y, z)-plane, as shown in Figure 7.

345 At high $|z|$, these flux ropes are quickly eroding under the effect of magnetic reconnection, as seen in Figure 4 as well as Supplementary Material Animation 1. This is the natural consequence of the purely southward conditions, which produce flux ropes with little axial field and therefore an overall leading-edge field that is mostly antiparallel to the lobe field and reconnects efficiently with it. As a result, no such dayside-originating flux ropes survive past $x = 0$ at high $|z|$, as shown in Figure 7.

At lower $|z|$ and larger $|y|$, the flow advects these flux ropes further along the flanks of the magnetopause, as showcased in
350 Figures 3, 5 and Supplementary Material Animation 2, as well as Figure 6. When following the evolution of such flux ropes, it is notable that any section of the flux rope presenting a magnetic field configuration antiparallel to the lobe magnetic field will erode away due to magnetic reconnection. This can be seen as the disappearance of the trailing section of the flux rope tracked in Figure 6(b), which has reconnected with the antiparallel magnetic field of the northern magnetotail lobe. It is also evidenced by the gradual decrease in the z-range in which flux ropes occur further downstream, shown in Figure 7. An exception is the

flux rope of Figure 5, which is seen as low as $z = -11\,R_{\mathrm{E}}$. Its leading section is oriented such that its field is mostly parallel with the southern lobe magnetic field, so it is not expected to significantly erode unless it were to advect towards the northern lobe and then reconnect.

Flux ropes have been observed in the far tail at $x = -67\,R_{\mathrm{E}}$ (Eastwood et al., 2012), albeit not very often. One obvious reason for the low number of reported far tail magnetosheath flux rope observations is the paucity of measurements in that region of geospace due to the orbital configuration of most spacecraft missions. An exception is the Acceleration, Reconnection, Turbulence, and Electrodynamics of the Moon's Interaction with the Sun mission (ARTEMIS, Sibeck et al., 2011) used by Eastwood et al. (2012) to observe these far tail flux ropes. The conditions in the present work lead to the formation of flux ropes on the dayside with an axis mostly parallel to the (x, y)-plane that are prone to reconnecting rapidly with the lobe magnetic field. The surviving ones such as the flux rope in Figure 6 would be extremely difficult to observe due to their axis being parallel to the plasma flow in the $-x$-direction, precluding the observation of the bipolar signature of the transverse magnetic field. It is therefore possible that such x-aligned magntosheath flux ropes are common, but difficult to detect. In conditions with significant IMF B_y, flux ropes may form in orientations more favourable for subsequent observations, such as in the event of Eastwood et al. (2012). In that event, it could be speculated that the lower portion of the flux rope in their Figure 7 might have eroded against the southern lobe field and that the flux rope was better preserved at the location of the ARTEMIS P1 spacecraft near the tail current sheet. However the authors also refer to conditions such as the fast shear flow between the magnetosheath and the lobe in the far tail region, which can suppress reconnection and help in preserving flux ropes in the tail (La Belle-Hamer et al., 1995; Cassak, 2011).

It will be the subject of future investigations using this novel flux rope detection method to study the global evolution of flux ropes under different IMF conditions. Once such a set of simulation datasets presenting a variety of geomagnetic and upstream conditions is available, it may become feasible to provide quantitative predictions on the occurrence rate of such low-latitude, flow-aligned, far-tail flux ropes, yet such a prediction would be perilous on the basis of the present simulation only. Another approach that may be considered, and would require a separate analysis, is to follow the approach developed by Grandin et al. (2024); Guo et al. (2024) who quantified the potential signature of dayside FTEs in soft X-ray observations. The Solar wind Magnetosphere Ionosphere Link Explorer (SMILE Branduardi-Raymont et al., 2018) and Lunar Environment heliospheric X-ray Imager (LEXI Walsh et al., 2024) missions will produce soft X-ray images from the emissions generated by charge-exchange reactions in near-Earth space (see Sibeck et al., 2018, for a review on the technique). SMILE will have a vantage point from "above the poles" with its eccentric, highly inclined orbit, while LEXI will observe from the surface of the Moon. Both will thus provide complementary and unprecedented observations, which may help in observing flux ropes in and around the magnetosphere more comprehensively than has been possible hitherto.

5.2 Flux ropes and O-line topology

In parallel to the generic flux rope detection method presented in this work, Alho et al. (2024) developed a local method determining the spatial location of lines where the magnetic field is in the so-called X- and O-line configurations, using a combination of the MGA and MDD techniques. X-lines are the site of magnetic reconnection when a non-zero rate of energy

conversion and field topology change is observed. O-lines can be interpreted as the core of magnetic flux ropes. As the method
uses derivatives of the magnetic field in a local coordinate system, it yields the essentially one-dimensional axis of flux ropes.
In order to identify a flux rope based on the O-lines yielded by that method, field lines could be traced in the neighbourhood
of said O-lines, for example. In the case of larger flux ropes where the axial region of 'straight' field lines is wider than a
one-dimensional line, the Alho et al. (2024) method might not yield a clear O-line. On the other hand, the method described
in the present work does not necessarily detect the actual core of flux ropes. In the case of a perfectly zero axial field, the
tracing would likely not succeed on a discrete grid, whereas in the case of non-zero axial field R_c could become very large and
tracing proceed to overly large distances. The method will however detect neighbouring regions surrounding the core reliably,
as shown in this work.

Although as explained in Section 2 the detection method is designed to be independent of specific spatial scales, one never-
theless has to set the $L_{\max}$ parameter, which defines the maximum distance tracing is allowed to proceed forward and backward
along the field line. Of course $R_{\max}$, the maximum extent away from the staring point allowed for flux rope detection, is a
parameter too but it cannot be larger than $L_{\max}$ and should not be set too small so that the optimal R_{cutoff} can be deter-
mined for the subsequent studies at hand. By setting the $L_{\max}$ parameter to $12\,R_c \approx 4\pi\,R_c$, an a priori decision is made to
search for well-formed flux ropes with the magnetic field clearly winding around their axis. This naturally includes FTEs at
the magnetopause and magnetotail plasmoids (see Section 2). Setting lower values for $L_{\max}$ increases the likelihood of false
positive identifications, namely regions of generally bent or curved magnetic field such as current sheets, which are however
not necessarily winding into flux rope structures. Additionally, at the chosen level of $R_{\mathrm{cutoff}} = 7\,R_c$, it is visible in Figure 4
and Supplementary Material Animation 1 that all detected flux rope regions (green circles) include an O-line (yellow squares).
However, a number of O-lines are seen outside of detected flux rope regions. While there might be positive flux rope detections
just outside the plane of the respective panel, it is more likely that such isolated O-lines exhibit the O-line topology locally
but not at a sufficiently large scale with respect to the grid resolution to be picked up by the tracing method of this work with
$L_{\max} = 12\,R_c \approx 4\pi\,R_c$ and $R_{\mathrm{cutoff}} = 7\,R_c$.

These two methods are therefore complementary in their approach and results. The local method of Alho et al. (2024) detects
all O-line configurations regardless of the wider surrounding magnetic field configuration, whereas this work demonstrates a
field-tracing method geared towards identifying well-formed flux ropes of any sufficiently-resolved scale.

5.3 Higher guide field configurations

In this work, flux ropes are identified in a simulation setup featuring purely southward IMF and no dipole tilt. These conditions
lead to magnetopause reconnection with (nearly) zero guide field and therefore the formation of flux ropes with low axial
field. When introducing an IMF B_y component, magnetopause reconnection will occur in different locations (e.g., Trattner
et al., 2021), leading to a different sectorial distribution of the flux ropes but also potentially more complex topologies of
flux ropes (Fargette et al., 2020). This will also have an impact on the distribution of flux ropes further down the flanks and
their reconnection with the lobes or their survival down the tail. Another aspect of the introduction of a non-zero B_y is that
this introduces a guide field to the reconnection geometry. In (mostly) antiparallel reconnection as in this work, flux ropes

consist of magnetic field that is close to perpendicular to the flux rope axis. With a stronger guide field, the flux ropes will be less tightly-wound. The magnetic field at the core of such flux ropes is then oriented more parallel to the flux rope axis. This

425 case is less favourable to detection by the present method. However the magnetic field is still wrapping around and thus more perpendicular to the axis of the flux rope in outer layers, allowing detection albeit potentially requiring a higher R_{cutoff}.

It is possible that a higher R_{cutoff} is needed to identify all flux ropes in such higher guide field configurations. Even though the method presented in this work might not be able to detect all cells at the core of a flux rope with stronger axial field, it should nevertheless detect the parts of the structure surrounding the core, allowing identification of the flux rope.

430 6   Conclusions

We present a new method to detect flux ropes at runtime in large-scale numerical simulations of the Earth's magnetosphere. The method is implemented in the hybrid-Vlasov model Vlasiator. Using only magnetic field line tracing, the method detects flux ropes of any scale and orientation as structures where the magnetic field is sufficiently wound up. The method does not require a priori identification of, for instance, the magnetopause or the tail current sheet or bipolar magnetic field profiles. It

435 is thus more general and robust than previously published flux rope detection methods, and may find applications beyond the specific implementation used in this study. The key aspect of the method is to scale the search criteria by the local curvature radius of the magnetic field, which enables an identification of flux ropes that is agnostic to their absolute spatial scale.

We apply the flux rope detection method to a simulation of the magnetosphere under purely southward IMF, which produces abundant FTEs generated by dayside magnetic reconnection as well as magnetotail plasmoids generated by tail current sheet

440 reconnection. We then analyse in particular the global evolution of FTE flux ropes along the magnetopause, which is charac- terised by rapid erosion due to reconnection with the shearing magnetic field component of the cusp and lobe magnetic field. This leads to the consequence that no FTEs survive for more than a few Earth radii tailward from the cusp regions. Lower on the flanks however, FTE flux ropes without shear component are advected with the magnetosheath flow into the far tail and preserve their integrity for tens of Earth radii.

445 Future research will include the analysis of the formation and evolution of tail plasmoids, which is not addressed in this work. Furthermore, building upon the flux rope detection capabilities demonstrated here, following studies will be able to quantitatively study the evolution of flux ropes as pioneered in earlier simulation and observational works (e.g. Akhavan-Tafti et al., 2019; Hoilijoki et al., 2019; Paul et al., 2023). Simulations with different upstream conditions will shed more light onto the global behaviour of FTEs, potentially allowing the investigation of the interplay of flux ropes and the Kelvin-Helmholtz

450 instability at the magnetopause, or the suppression of lobe reconnection under different magnetospheric or upstream conditions. Finally, beyond the arguably difficult in situ observation of far-tail flux ropes, it also remains to be quantified whether soft X- ray imagers like SMILE and LEXI will be able to observe them, as has been suggested for the observation of dayside FTEs with SMILE (Grandin et al., 2024; Guo et al., 2024).

Video supplement. The animated version of Figure 4 is presented in Supplementary Material Animation 1. The animated version of Figure
5 is presented in Supplementary Material Animation 2.

Author contributions. Conceptualisation: YP, MA, KH; Data curation: YP, JS, MA; Formal analysis: YP, MA; Funding acquisition: YP,
460 MP; Investigation: YP, KH; Methodology: YP, MA, KH; Project administration: YP, MP; Resources: YP, MP, MB, UG; Software: YP, UG,
KP, MB, MA, LP; Supervision: YP, MP; Verification and validation: YP; Visualisation: YP, LP; Writing — original draft preparation: YP;
Writing — review and editing: all co-authors.

Competing interests. Some authors are members of the editorial board of Annales Geophysicae.

References

Akhavan-Tafti, M., Slavin, J. A., Eastwood, J. P., Cassak, P. A., and Gershman, D. J.: MMS Multi-Point Analysis of FTE Evolution: Physical
480   Characteristics and Dynamics, Journal of Geophysical Research: Space Physics, 124, 5376–5395, https://doi.org/10.1029/2018JA026311,
       2019.

Akhavan-Tafti, M., Palmroth, M., Slavin, J., Battarbee, M., Ganse, U., Grandin, M., Le, G., Gershman, D., Eastwood, J., and Stawarz, J.:
       Comparative Analysis of the Vlasiator Simulations and MMS Observations of Multiple X-Line Reconnection and Flux Transfer Events,
       Journal of Geophysical Research: Space Physics, https://doi.org/10.1029/2019JA027410, 2020.

485   Ala-Lahti, M., Pulkkinen, T. I., Pfau-Kempf, Y., Grandin, M., and Palmroth, M.: Energy Flux Through the Magne-
       topause During Flux Transfer Events in Hybrid-Vlasov 2D Simulations, Geophysical Research Letters, 49, e2022GL100 079,
       https://doi.org/10.1029/2022GL100079, 2022.

Alho, M., Cozzani, G., Zaitsev, I., Kebede, F. T., Ganse, U., Battarbee, M., Bussov, M., Dubart, M., Hoilijoki, S., Kotipalo, L., Papadakis, K.,
       Pfau-Kempf, Y., Suni, J., Tarvus, V., Workayehu, A., Zhou, H., and Palmroth, M.: Finding reconnection lines and flux rope axes via local
490   coordinates in global ion-kinetic magnetospheric simulations, Annales Geophysicae, 42, 145–161, https://doi.org/10.5194/angeo-42-145-
       2024, 2024.

Balsara, D. S.: Divergence-free reconstruction of magnetic fields and WENO schemes for magnetohydrodynamics, Journal of Computational
       Physics, 228, 5040–5056, https://doi.org/10.1016/j.jcp.2009.03.038, 2009.

Battarbee, M., Alho, M., Pfau-Kempf, Y., Ganse, U., Grandin, M., Kotipalo, L., Papadakis, K., Jarvinen, R., Pänkäläinen, L., Suni, J., von
495   Alfthan, S., Tarvus, V., Zaitsev, I., Tao, S., Horaites, K., Turc, L., Tesema, F. K., Zhou, H., Honkonen, I., Brito, T., Lalagüe, A., Siljamo,
       S., and Reimi, J.: analysator, https://doi.org/10.5281/zenodo.4462514, 2024.

Bowers, C. F., Slavin, J. A., DiBraccio, G. A., Poh, G., Hara, T., Xu, S., and Brain, D. A.: MAVEN Survey of Magnetic Flux Rope Properties
       in the Martian Ionosphere: Comparison With Three Types of Formation Mechanisms, Geophysical Research Letters, 48, e2021GL093 296,
       https://doi.org/10.1029/2021GL093296, 2021.

500   Brain, D. A., Baker, A. H., Briggs, J., Eastwood, J. P., Halekas, J. S., and Phan, T.-D.: Episodic detachment of Martian crustal magnetic fields
       leading to bulk atmospheric plasma escape, Geophysical Research Letters, 37, https://doi.org/10.1029/2010GL043916, 2010.

Branduardi-Raymont, G., Wang, C., Escoubet, C., Adamovic, M., Agnolon, D., Berthomier, M., Carter, J., Chen, W., Colangeli, L., Collier,
       M., Connor, H., Dai, L., Dimmock, A., Djazovski, O., Donovan, E., Eastwood, J., Enno, G., Giannini, F., Huang, L., Kataria, D., Kuntz, K.,
       Laakso, H., Li, J., Li, L., Lui, T., Loicq, J., Masson, A., Manuel, J., Parmar, A., Piekutowski, T., Read, A., Samsonov, A., Sembay, S., Raab,
505   W., Ruciman, C., Shi, J., Sibeck, D., Spanswick, E., Sun, T., Symonds, K., Tong, J., Walsh, B., Wei, F., Zhao, D., Zheng, J., Zhu, X., and
       Zhu, Z.: SMILE definition study report, European Space Agency, ESA/SCI, 1, https://doi.org/10.5270/esa.smile.definition_study_report-
       2018-12, 2018.

Brenner, A., Pulkkinen, T. I., Al Shidi, Q., and Toth, G.: Stormtime Energetics: Energy Transport Across the Magnetopause in a Global MHD
       Simulation, Frontiers in Astronomy and Space Sciences, 8, https://doi.org/10.3389/fspas.2021.756732, 2021.

510   Cartwright, M. L. and Moldwin, M. B.: Heliospheric evolution of solar wind small-scale magnetic flux ropes, Journal of Geophysical
       Research: Space Physics, 115, https://doi.org/10.1029/2009JA014271, 2010.

Cassak, P. A.: Theory and simulations of the scaling of magnetic reconnection with symmetric shear flow, Physics of Plasmas, 18, 072 106,
       https://doi.org/10.1063/1.3602859, 2011.

Childs, H., Brugger, E., Whitlock, B., Meredith, J., Ahern, S., Pugmire, D., Biagas, K., Miller, M. C., Harrison, C., Weber, G. H., Krishnan, H., Fogal, T., Sanderson, A., Garth, C., Bethel, E. W., Camp, D., Rubel, O., Durant, M., Favre, J. M., and Navratil, P.: High Performance Visualization–Enabling Extreme-Scale Scientific Insight, https://doi.org/10.1201/b12985, 2012.

DiBraccio, G. A. and Gershman, D. J.: Voyager 2 constraints on plasmoid-based transport at Uranus, Geophysical Research Letters, 46, 10 710–10 718, https://doi.org/10.1029/2019GL083909, 2019.

Eastwood, J. P. and Kiehas, S. A.: Origin and Evolution of Plasmoids and Flux Ropes in the Magnetotails of Earth and Mars, chap. 16, pp. 269–287, American Geophysical Union (AGU), ISBN 9781118842324, https://doi.org/10.1002/9781118842324.ch16, 2015.

Eastwood, J. P., Phan, T. D., Fear, R. C., Sibeck, D. G., Angelopoulos, V., Øieroset, M., and Shay, M. A.: Survival of flux transfer event (FTE) flux ropes far along the tail magnetopause, Journal of Geophysical Research: Space Physics, 117, https://doi.org/10.1029/2012JA017722, 2012.

Edberg, N. J. T., Alho, M., André, M., Andrews, D. J., Behar, E., Burch, J. L., Carr, C. M., Cupido, E., Engelhardt, I. A. D., Eriksson, A. I., Glassmeier, K.-H., Goetz, C., Goldstein, R., Henri, P., Johansson, F. L., Koenders, C., Mandt, K., Möstl, C., Nilsson, H., Odelstad, E., Richter, I., Simon Wedlund, C., Stenberg Wieser, G., Szego, K., Vigren, E., and Volwerk, M.: CME impact on comet 67P/Churyumov-Gerasimenko, Monthly Notices of the Royal Astronomical Society, 462, S45–S56, https://doi.org/10.1093/mnras/stw2112, 2016.

Elphic, R. C. and Russell, C. T.: Magnetic flux ropes in the Venus ionosphere: Observations and models, Journal of Geophysical Research: Space Physics, 88, 58–72, https://doi.org/10.1029/JA088iA01p00058, 1983.

Fargette, N., Lavraud, B., Øieroset, M., Phan, T. D., Toledo-Redondo, S., Kieokaew, R., Jacquey, C., Fuselier, S. A., Trattner, K. J., Petrinec, S., Hasegawa, H., Garnier, P., Génot, V., Lenouvel, Q., Fadanelli, S., Penou, E., Sauvaud, J.-A., Avanov, D. L. A., Burch, J., Chandler, M. O., Coffey, V. N., Dorelli, J., Eastwood, J. P., Farrugia, C. J., Gershman, D. J., Giles, B. L., Grigorenko, E., Moore, T. E., Paterson, W. R., Pollock, C., Saito, Y., Schiff, C., and Smith, S. E.: On the Ubiquity of Magnetic Reconnection Inside Flux Transfer Event-Like Structures at the Earth's Magnetopause, Geophysical Research Letters, 47, e2019GL086 726, https://doi.org/10.1029/2019GL086726, 2020.

Fermo, R. L., Drake, J. F., and Swisdak, M.: Secondary Magnetic Islands Generated by the Kelvin-Helmholtz Instability in a Reconnecting Current Sheet, Physical Review Letters, 108, 255 005, https://doi.org/10.1103/PhysRevLett.108.255005, 2012.

Ganse, U., Koskela, T., Battarbee, M., Pfau-Kempf, Y., Papadakis, K., Alho, M., Bussov, M., Cozzani, G., Dubart, M., George, H., Gordeev, E., Grandin, M., Horaites, K., Suni, J., Tarvus, V., Kebede, F. T., Turc, L., Zhou, H., and Palmroth, M.: Enabling technology for global 3D + 3V hybrid-Vlasov simulations of near-Earth space, Physics of Plasmas, 30, https://doi.org/10.1063/5.0134387, 2023.

Ganse, U., Pfau-Kempf, Y., Zhou, H., Juusola, L., Workayehu, A., Kebede, F., Papadakis, K., Grandin, M., Alho, M., Battarbee, M., Dubart, M., Kotipalo, L., Lalagüe, A., Suni, J., Horaites, K., and Palmroth, M.: The Vlasiator 5.2 Ionosphere – Coupling a magnetospheric hybrid-Vlasov simulation with a height-integrated ionosphere model, Geoscientific Model Development Discussions, 2024, 1–28, https://doi.org/10.5194/gmd-2024-101, 2024.

Grandin, M., Turc, L., Battarbee, M., Ganse, U., Johlander, A., Pfau-Kempf, Y., Dubart, M., and Palmroth, M.: Hybrid-Vlasov simulation of auroral proton precipitation in the cusps: Comparison of northward and southward interplanetary magnetic field driving, Journal of space weather and space climate, 10, https://doi.org/10.1051/swsc/2020053, 2020.

Grandin, M., Luttikhuis, T., Battarbee, M., Cozzani, G., Zhou, H., Turc, L., Pfau-Kempf, Y., George, H., Horaites, K., Gordeev, E., Ganse, U., Papadakis, K., Alho, M., Tesema, F., Suni, J., Dubart, M., Tarvus, V., and Palmroth, M.: First 3D hybrid-Vlasov global simulation of auroral proton precipitation and comparison with satellite observations, Journal of Space Weather Space Climate, 13, 20, https://doi.org/10.1051/swsc/2023017, 2023.

Annales
Geophysicae
Discussions

Grandin, M., Connor, H. K., Hoilijoki, S., Battarbee, M., Pfau-Kempf, Y., Ganse, U., Papadakis, K., and Palmroth, M.: Hybrid-Vlasov simulation of soft X-ray emissions at the Earth's dayside magnetospheric boundaries, Earth and Planetary Physics, 8, 70–88, https://doi.org/10.26464/epp2023052, 2024.

555 Guo, J., Sun, T., Lu, S., Lu, Q., Lin, Y., Wang, X., Wang, C., Wang, R., and Huang, K.: Global hybrid simulations of soft X-ray emissions in the Earth's magnetosheath, Earth and Planetary Physics, 8, 47–58, https://doi.org/10.26464/epp2023053, 2024.

Haerendel, G., Paschmann, G., Sckopke, N., Rosenbauer, H., and Hedgecock, P. C.: The frontside boundary layer of the magnetosphere and the problem of reconnection, Journal of Geophysical Research: Space Physics, 83, 3195–3216, https://doi.org/10.1029/JA083iA07p03195, 1978.

560 Hara, T., Brain, D. A., Mitchell, D. L., Luhmann, J. G., Seki, K., Hasegawa, H., Mcfadden, J. P., Halekas, J. S., Espley, J. R., Harada, Y., Livi, R., DiBraccio, G. A., Connerney, J. E. P., Mazelle, C., Andersson, L., and Jakosky, B. M.: MAVEN observations of a giant ionospheric flux rope near Mars resulting from interaction between the crustal and interplanetary draped magnetic fields, Journal of Geophysical Research: Space Physics, 122, 828–842, https://doi.org/10.1002/2016JA023347, 2017a.

Hara, T., Harada, Y., Mitchell, D. L., DiBraccio, G. A., Espley, J. R., Brain, D. A., Halekas, J. S., Seki, K., Luhmann, J. G., McFadden, J. P.,
565 Mazelle, C., and Jakosky, B. M.: On the origins of magnetic flux ropes in near-Mars magnetotail current sheets, Geophysical Research Letters, 44, 7653–7662, https://doi.org/10.1002/2017GL073754, 2017b.

Hoilijoki, S., Ganse, U., Sibeck, D. G., Cassak, P. A., Turc, L., Battarbee, M., Fear, R. C., Blanco-Cano, X., Dimmock, A. P., Kilpua, E. K. J., Jarvinen, R., Juusola, L., Pfau-Kempf, Y., and Palmroth, M.: Properties of Magnetic Reconnection and FTEs on the Dayside Magnetopause With and Without Positive IMF Bx Component During Southward IMF, Journal of Geophysical Research: Space Physics,
570 124, 4037–4048, https://doi.org/10.1029/2019JA026821, 2019.

Huang, S., Zhao, P., He, J., Yuan, Z., Zhou, M., Fu, H., Deng, X., Pang, Y., Wang, D., Yu, X., Li, H., Torbert, R., and Burch, J.: A new method to identify flux ropes in space plasmas, Annales Geophysicae, 36, 1275–1283, https://doi.org/10.5194/angeo-36-1275-2018, 2018.

Isavnin, A., Kilpua, E., and Koskinen, H.: Grad–Shafranov Reconstruction of Magnetic Clouds: Overview and Improvements, Solar Physics, 273, 205—219, https://doi.org/10.1007/s11207-011-9845-z, 2011.

575 Isavnin, A., Vourlidas, A., and Kilpua, E.: Three-Dimensional Evolution of Flux-Rope CMEs and Its Relation to the Local Orientation of the Heliospheric Current Sheet, Solar Physics, 289, 2141—2156, https://doi.org/10.1007/s11207-013-0468-4, 2014.

Jackman, C. M., Slavin, J. A., Kivelson, M. G., Southwood, D. J., Achilleos, N., Thomsen, M. F., DiBraccio, G. A., Eastwood, J. P., Freeman, M. P., Dougherty, M. K., and Vogt, M. F.: Saturn's dynamic magnetotail: A comprehensive magnetic field and plasma survey of plasmoids and traveling compression regions and their role in global magnetospheric dynamics, Journal of Geophysical Research: Space Physics,
580 119, 5465–5494, https://doi.org/10.1002/2013JA019388, 2014.

Janvier, M., Démoulin, P., and Dasso, S.: In situ properties of small and large flux ropes in the solar wind, Journal of Geophysical Research: Space Physics, 119, 7088–7107, https://doi.org/10.1002/2014JA020218, 2014.

Jarvinen, R., Vainio, R., Palmroth, M., Juusola, L., Hoilijoki, S., Pfau-Kempf, Y., Ganse, U., Turc, L., and von Alfthan, S.: Ion Acceleration by Flux Transfer Events in the Terrestrial Magnetosheath, Geophysical Research Letters, 45, 1723–1731,
585 https://doi.org/10.1002/2017GL076192, 2018.

Jasinski, J. M., Slavin, J. A., Arridge, C. S., Poh, G., Jia, X., Sergis, N., Coates, A. J., Jones, G. H., and Waite Jr., J. H.: Flux transfer event observation at Saturn's dayside magnetopause by the Cassini spacecraft, Geophysical Research Letters, 43, 6713–6723, https://doi.org/10.1002/2016GL069260, 2016.

Annales
Geophysicae
Discussions

Open Access

EGU

Kieokaew, R., Lavraud, B., Fargette, N., Marchaudon, A., Génot, V., Jacquey, C., Gershman, D., Giles, B., Torbert, R., and Burch, J.:
590   Statistical Relationship Between Interplanetary Magnetic Field Conditions and the Helicity Sign of Flux Transfer Event Flux Ropes,
    Geophysical Research Letters, 48, e2020GL091 257, https://doi.org/10.1029/2020GL091257, 2021.

Kotipalo, L., Battarbee, M., Pfau-Kempf, Y., and Palmroth, M.: Physics-motivated Cell-octree Adaptive Mesh Refinement in the Vlasiator
    5.3 Global Hybrid-Vlasov Code, Geoscientific Model Development, 17, 6401–6413, https://doi.org/10.5194/gmd-17-6401-2024, 2024.

Kronberg, E. A., Woch, J., Krupp, N., Lagg, A., Khurana, K. K., and Glassmeier, K.-H.: Mass release at Jupiter: Substorm-like processes in
595   the Jovian magnetotail, Journal of Geophysical Research: Space Physics, 110, https://doi.org/10.1029/2004JA010777, 2005.

La Belle-Hamer, A. L., Otto, A., and Lee, L. C.: Magnetic reconnection in the presence of sheared flow and density asymmetry: Applications
    to the Earth's magnetopause, Journal of Geophysical Research: Space Physics, 100, 11 875–11 889, https://doi.org/10.1029/94JA00969,
    1995.

Liu, R.: Magnetic flux ropes in the solar corona: structure and evolution toward eruption, Research in Astronomy and Astrophysics, 20,
600   https://doi.org/10.1088/1674-4527/20/10/165, 2020.

Lowder, C. and Yeates, A.: Magnetic Flux Rope Identification and Characterization from Observationally Driven Solar Coronal Models, The
    Astrophysical Journal, 846, 106, https://doi.org/10.3847/1538-4357/aa86b1, 2017.

Lv, L., Pu, Z., and Xie, L.: Multiple magnetic topologies in flux transfer events: THEMIS measurements, Science China Technological
    Sciences, 59, 1283—-1293, https://doi.org/10.1007/s11431-016-6071-9, 2016.

605 MacTaggart, D., Prior, C., Raphaldini, B., Romano, P., and Guglielmino, S.: Direct evidence that twisted flux tube emergence creates solar
    active regions, Nature Communications, 12, https://doi.org/10.1038/s41467-021-26981-7, 2021.

Martin, C. J., Arridge, C. S., Badman, S. V., Russell, C. T., and Wei, H.: Distribution and Properties of Magnetic Flux Ropes in Titan's
    Ionosphere, Journal of Geophysical Research: Space Physics, 125, e2019JA027 570, https://doi.org/10.1029/2019JA027570, 2020.

McGregor, D. C., Kerr, S. E., and Krockenberger, A. K.: The distribution and abundance of an island population of Koalas (Phascolarctos
610   cinereus) in the far north of their geographic range, PLoS One, 8, e59 713, https://doi.org/10.1371/journal.pone.0059713, 2013.

Moldwin, M. B., Ford, S., Lepping, R., Slavin, J., and Szabo, A.: Small-scale magnetic flux ropes in the solar wind, Geophysical Research
    Letters, 27, 57–60, https://doi.org/10.1029/1999GL010724, 2000.

Palmroth, M., Hoilijoki, S., Juusola, L., Pulkkinen, T. I., Hietala, H., Pfau-Kempf, Y., Ganse, U., von Alfthan, S., Vainio, R., and
    Hesse, M.: Tail reconnection in the global magnetospheric context: Vlasiator first results, Annales Geophysicae, 35, 1269–1274,
615   https://doi.org/10.5194/angeo-35-1269-2017, 2017.

Palmroth, M., Ganse, U., Pfau-Kempf, Y., Battarbee, M., Turc, L., Brito, T., Grandin, M., Hoilijoki, S., Sandroos, A., and von Alfthan, S.:
    Vlasov methods in space physics and astrophysics, Living Reviews in Computational Astrophysics, 4, 1, https://doi.org/10.1007/s41115-
    018-0003-2, 2018.

Palmroth, M., Pulkkinen, T., Ganse, U., Pfau-Kempf, Y., Koskela, T., Zaitsev, I., Alho, M., Cozzani, G., Turc, L., Battarbee, M., Dubart,
620   M., George, H., Gordeev, E., Grandin, M., Horaites, K., Osmane, A., Papadakis, K., Suni, J., Tarvus, V., Zhou, H., and Naka-
    mura, R.: Magnetotail plasma eruptions driven by magnetic reconnection and kinetic instabilities, Nature Geoscience, 16, 570–576,
    https://doi.org/10.1038/s41561-023-01206-2, 2023.

Papadakis, K., Pfau-Kempf, Y., Ganse, U., Battarbee, M., Alho, M., Grandin, M., Dubart, M., Turc, L., Zhou, H., Horaites, K., Zaitsev, I.,
    Cozzani, G., Bussov, M., Gordeev, E., Tesema, F., George, H., Suni, J., Tarvus, V., and Palmroth, M.: Spatial filtering in a 6D hybrid-
625   Vlasov scheme to alleviate adaptive mesh refinement artifacts: a case study with Vlasiator (versions 5.0, 5.1, and 5.2.1), Geoscientific
    Model Development, 15, 7903–7912, https://doi.org/10.5194/gmd-15-7903-2022, 2022.

Paul, A., Vaidya, B., and Strugarek, A.: A Volumetric Study of Flux Transfer Events at the Dayside Magnetopause, The Astrophysical Journal, 938, 130, https://doi.org/10.3847/1538-4357/ac8eb5, 2022.

Paul, A., Strugarek, A., and Vaidya, B.: Global-MHD Simulations Using MagPIE: Impact of Flux Transfer Events on the Ionosphere, Journal
630   of Geophysical Research: Space Physics, 128, e2023JA031 718, https://doi.org/10.1029/2023JA031718, 2023.

Pfau-Kempf, Y., Hietala, H., Milan, S. E., Juusola, L., Hoilijoki, S., Ganse, U., von Alfthan, S., and Palmroth, M.: Evidence for transient, local ion foreshocks caused by dayside magnetopause reconnection, Annales Geophysicae, 34, 943–959, https://doi.org/10.5194/angeo-34-943-2016, 2016.

Pfau-Kempf, Y., Palmroth, M., Johlander, A., Turc, L., Alho, M., Battarbee, M., Dubart, M., Grandin, M., and Ganse, U.: Hybrid-Vlasov
635   modeling of three-dimensional dayside magnetopause reconnection, Physics of Plasmas, 27, https://doi.org/10.1063/5.0020685, 2020.

Pfau-Kempf, Y., von Alfthan, S., Ganse, U., Sandroos, A., Battarbee, M., Koskela, T., Hannuksela, O., Honkonen, I., Papadakis, K., Kotipalo, L., Zhou, H., Grandin, M., Pokhotelov, D., and Alho, M.: fmihpc/vlasiator: Vlasiator, https://doi.org/10.5281/zenodo.3640593, 2024.

Picone, J. M., Hedin, A. E., Drob, D. P., and Aikin, A. C.: NRLMSISE-00 empirical model of the atmosphere: Statistical comparisons and scientific issues, Journal of Geophysical Research: Space Physics, 107, SIA 15–1–SIA 15–16,
640   https://doi.org/https://doi.org/10.1029/2002JA009430, 2002.

Press, W., Teukolsky, S., Vetterling, W., and Flannery, B.: Numerical Recipes: The Art of Scientific Computing, Third Edition, chap. 17, Cambridge University Press, ISBN 978-0-521-88068-8, 2011.

Rijnbeek, R. and Cowley, S.: Magnetospheric flux erosion events are flux transfer events, Nature, 309, 135—138, https://doi.org/10.1038/309135a0, 1984.

645 Ripperda, B., Liska, M., Chatterjee, K., Musoke, G., Philippov, A., Markoff, S., Tchekhovskoy, A., and Younsi, Z.: Black Hole Flares: Ejection of Accreted Magnetic Flux through 3D Plasmoid-mediated Reconnection, The Astrophysical Journal Letters, 924, https://doi.org/10.3847/2041-8213/ac46a1, 2022.

Romanelli, N., DiBraccio, G. A., Modolo, R., Connerney, J. E. P., Ebert, R. W., Martos, Y. M., Weber, T., Espley, J. R., Kurth, W. S., Allegrini, F., Valek, P., and Bolton, S. J.: Juno Magnetometer Observations at Ganymede: Comparisons With a Global Hybrid Simulation and
650   Indications of Magnetopause Reconnection, Geophysical Research Letters, 49, e2022GL099 545, https://doi.org/10.1029/2022GL099545, 2022.

Runov, A., Grandin, M., Palmroth, M., Battarbee, M., Ganse, U., Hietala, H., Hoilijoki, S., Kilpua, E., Pfau-Kempf, Y., Toledo-Redondo, S., Turc, L., and Turner, D.: Ion distribution functions in magnetotail reconnection: global hybrid-Vlasov simulation results, Annales Geophysicae, 39, 599–612, https://doi.org/10.5194/angeo-39-599-2021, 2021.

655 Russell, C. T. and Elphic, R. C.: Initial ISEE magnetometer results: magnetopause observations, Space Science Reviews, 22, 681—715, https://doi.org/10.1007/BF00212619, 1978.

Sarkango, Y., Slavin, J. A., Jia, X., DiBraccio, G. A., Gershman, D. J., Connerney, J. E. P., Kurth, W. S., and Hospodarsky, G. B.: Juno Observations of Ion-Inertial Scale Flux Ropes in the Jovian Magnetotail, Geophysical Research Letters, 48, e2020GL089 721, https://doi.org/10.1029/2020GL089721, 2021.

660 Sarkango, Y., Slavin, J. A., Jia, X., DiBraccio, G. A., Clark, G. B., Sun, W., Mauk, B. H., Kurth, W. S., and Hospodarsky, G. B.: Properties of Ion-Inertial Scale Plasmoids Observed by the Juno Spacecraft in the Jovian Magnetotail, Journal of Geophysical Research: Space Physics, 127, e2021JA030 181, https://doi.org/10.1029/2021JA030181, 2022.

Sibeck, D. G., Angelopoulos, V., Brain, D. A., Delory, G. T., Eastwood, J. P., Farrell, W. M., Grimm, R. E., Halekas, J. S., Hasegawa, H.,
Hellinger, P., Khurana, K. K., Lillis, R. J., Øieroset, M., Phan, T.-D., Raeder, J., Russell, C. T., Schriver, D., Slavin, J. A., M., T. P., and

665 Weygand, J. M.: ARTEMIS Science Objectives, Space Science Reviews, 165, 59–91, https://doi.org/10.1007/s11214-011-9777-9, 2011.

Sibeck, D. G., Allen, R., Aryan, H., Bodewits, D., Brandt, P., Branduardi-Raymont, G., Brown, G., Carter, J. A., Collado-Vega, Y. M.,
Collier, M. R., Connor, H. K., Cravens, T. E., Ezoe, Y., Fok, M.-C., Galeazzi, M., Gutynska, O., Holmström, M., S.-Y. Hsieh and,
K. I., Koutroumpa, D., Kuntz, K. D., Leutenegger, M., Miyoshi, Y., Porter, F. S., Purucker, M. E., Read, A. M., Raeder, J., Robert-
son, I. P., Samsonov, A. A., Sembay, S., Snowden, S. L., Thomas, N. E., von Steiger, R., Walsh, B. M., and Wing, S.: Imaging

670 Plasma Density Structures in the Soft X-Rays Generated by Solar Wind Charge Exchange with Neutrals, Space Science Reviews, 214,
https://doi.org/10.1007/s11214-018-0504-7, 2018.

Slavin, J. A., Acuña, M. H., Anderson, B. J., Baker, D. N., Benna, M., Boardsen, S. A., Gloeckler, G., Gold, R. E., Ho, G. C., Korth, H., Krim-
igis, S. M., McNutt, R. L., Raines, J. M., Sarantos, M., Schriver, D., Solomon, S. C., Trávníček, P., and Zurbuchen, T. H.: MESSENGER
Observations of Magnetic Reconnection in Mercury's Magnetosphere, Science, 324, 606–610, https://doi.org/10.1126/science.1172011,

675 2009.

Smith, A. W., Sun, W., Slavin, J. A., and Rae, I. J.: Ion-Scale Magnetic Flux Ropes and Loops in Earth's Magnetotail: An Automated,
Comprehensive Survey of MMS Data Between 2017 and 2022, Journal of Geophysical Research: Space Physics, 129, e2023JA032 231,
https://doi.org/10.1029/2023JA032231, 2024.

Sun, W. J., Fu, S. Y., Slavin, J. A., Raines, J. M., Zong, Q. G., Poh, G. K., and Zurbuchen, T. H.: Spatial distribution of Mercury's

680 flux ropes and reconnection fronts: MESSENGER observations, Journal of Geophysical Research: Space Physics, 121, 7590–7607,
https://doi.org/10.1002/2016JA022787, 2016.

Tesema, F., Palmroth, M., Turc, L., Zhou, H., Cozzani, G., Alho, M., Pfau-Kempf, Y., Horaites, K., Zaitsev, I., Grandin, M., Battarbee, M.,
Ganse, U., Workayehu, A., Suni, J., Papadakis, K., Dubart, M., and Tarvus, V.: Dayside Pc2 Waves Associated With Flux Transfer Events
in a 3D Hybrid-Vlasov Simulation, Geophysical Research Letters, 51, e2023GL106 756, https://doi.org/10.1029/2023GL106756, 2024.

685 Trattner, K. J., Petrinec, S. M., and Fuselier, S. A.: The Location of Magnetic Reconnection at Earth's Magnetopause, Space Science Reviews,
217, https://doi.org/10.1007/s11214-021-00817-8, 2021.

Turk, M. J., Smith, B. D., Oishi, J. S., Skory, S., Skillman, S. W., Abel, T., and Norman, M. L.: yt: A Multi-code Analysis Toolkit for
Astrophysical Simulation Data, The Astrophysical Journal Supplement Series, 192, 9, https://doi.org/10.1088/0067-0049/192/1/9, 2011.

Vogt, M. F., Jackman, C. M., Slavin, J. A., Bunce, E. J., Cowley, S. W. H., Kivelson, M. G., and Khurana, K. K.: Structure

690 and statistical properties of plasmoids in Jupiter's magnetotail, Journal of Geophysical Research: Space Physics, 119, 821–843,
https://doi.org/10.1002/2013JA019393, 2014.

von Alfthan, S., Pokhotelov, D., Kempf, Y., Hoilijoki, S., Honkonen, I., Sandroos, A., and Palmroth, M.: Vlasiator: first kinetic
global hybrid-Vlasov simulation code for modeling space plasma, Journal of Atmospheric and Solar-Terrestrial Physics, 120, 24–35,
https://doi.org/10.1016/j.jastp.2014.08.012, 2014.

695 Wagner, A., Bourgeois, S., Kilpua, E. K. J., Sarkar, R., Price, D. J., Kumari, A., Pomoell, J., Poedts, S., Barata, T., Erdélyi, R., Oliveira,
O., and Gafeira, R.: The automatic identification and tracking of coronal flux ropes – II. New mathematical morphology-based flux rope
extraction method and deflection analysis, Astronomy & Astrophysics, 683, A39, https://doi.org/10.1051/0004-6361/202348113, 2024.

Walsh, B. M., Kuntz, K. D., Busk, S., Cameron, T., Chornay, D., Chuchra, A., Collier, M. R., Connor, C., Connor, H. K., Cravens, T. E.,
Dobson, N., Galeazzi, M., Kim, H., Kujawski, J., U, C. K. P., Porter, F. S., Naldoza, V., Nutter, R., Qudsi, R., Sibeck, D. G., Sembay, S.,

700   Shoemaker, M., Simms, K., Thomas, N. E., Atz, E., and Winkert, G.: The Lunar Environment Heliophysics X-ray Imager (LEXI) Mission, Space Science Reviews, 220, https://doi.org/10.1007/s11214-024-01063-4, 2024.

Wang, W., Liu, R., Wang, Y., Hu, Q., Shen, C., Jiang, C., and Zhu, C.: Buildup of a highly twisted magnetic flux rope during a solar eruption, Nature Communications, 8, https://doi.org/10.1038/s41467-017-01207-x, 2017.

Wang, Y. L., Elphic, R. C., Lavraud, B., Taylor, M. G. G. T., Birn, J., Russell, C. T., Raeder, J., Kawano, H., and Zhang, X. X.: Dependence
705   of flux transfer events on solar wind conditions from 3 years of Cluster observations, Journal of Geophysical Research: Space Physics, 111, https://doi.org/10.1029/2005JA011342, 2006.

Xu, S., Liemohn, M. W., Dong, C., Mitchell, D. L., Bougher, S. W., and Ma, Y.: Pressure and ion composition boundaries at Mars, Journal of Geophysical Research: Space Physics, 121, 6417–6429, https://doi.org/10.1002/2016JA022644, 2016.

Zhang, T. L., Baumjohann, W., Teh, W. L., Nakamura, R., Russell, C. T., Luhmann, J. G., Glassmeier, K. H., Dubinin, E., Wei, H. Y., Du,
710   A. M., Lu, Q. M., Wang, S., and Balikhin, M.: Giant flux ropes observed in the magnetized ionosphere at Venus, Geophysical Research Letters, 39, https://doi.org/10.1029/2012GL054236, 2012.

Zhong, J., Lee, L.-C., Slavin, J. A., Zhang, H., and Wei, Y.: MESSENGER Observations of Reconnection in Mercury's Magnetotail Under Strong IMF Forcing, Journal of Geophysical Research: Space Physics, 128, e2022JA031 134, https://doi.org/10.1029/2022JA031134, 2023.

715 Zhou, M., Pang, Y., Deng, X., Huang, S., and Lai, X.: Plasma physics of magnetic island coalescence during magnetic reconnection, Journal of Geophysical Research: Space Physics, 119, 6177–6189, https://doi.org/10.1002/2013JA019483, 2014.